SUMMARY REPORT

1 June 1969 to 31 May 1970

MATERIAL BEHAVIOR IN HIGH SPEED IMPACT

J. Asay, J. E. Flinn, J. W. Forbes
R. H. Mitchell & G. E. Duvall

Contract No.
F 44620-67-C-0087

WSU SDL 70-03
July 1970

Research sponsored by the U. S. Air Force Office of Scientific Research (Advanced Research Projects Agency), Arlington, Virginia

SUMMARY REPORT

1 June 1969 to 31 May 1970

ARPA Order Number:	985
Program Code Number:	7D10
Name of Contractor:	Washington State University
Date of Contract:	1 June 1967
Amount of Contract:	$274,112.00
Contract Number:	F44620-67-C-0087
Principal Investigator:	Professor George E. Duvall Phone: (509) 335-3310
Contract Expiration Date:	31 May 1970
Project Scientist:	Professor George E. Duvall Phone: (509) 335-3310
Title:	Material Behavior in High Speed Impact

FOREWORD

This Summary Report is in the nature of a progress report of ongoing work some of which is nearing completion. Data and speculations are tentative at this stage, however, and care should be exercised by the reader in quoting from this report.

ABSTRACT

This report consists of five sections which are more or less independent. The first is a study of the dynamics of dislocation motion and multiplication based on elastic precursor decay in LiF. Gilman's simple theory applied in a straightforward way does not describe the experimental data. In order to fit the data the dislocation density must be increased beyond the measured value by three or four orders of magnitude and the drag stress must be increased beyond Gilman's value by up to one order of magnitude. The possibility that Mg impurities play a role in the process is examined and the effects of vacancies produced by nuclear irradiation is considered. Alternative formulations of the decay theory are discussed and the possibility of multiplication in the elastic wave front is examined.

In Section II plans and progress are described for a direct experimental measurement of the threshold dynamic stress and time for dislocation multiplication in LiF. The experiments require production of dynamic uniaxial strain conditions in the sample via shock waves induced by a projectile accelerated by gravity. Low projectile velocity places very stringent requirements on mechanical tolerances and considerable trouble has been experienced with the apparatus. Prospects for overcoming these look bright.

Section III contains theoretical procedures for converting the current output of quartz gauges to stress in materials which produce double shock waves because of dynamic failure or phase transitions. These

procedures are used in Section IV to interpret shock measurements on CdS-lucite mixtures. CdS is known to have a phase transition at about 27 kbars, and this experiment is intended to study the dynamics of transition in a near-hydrostatic environment provided by the Lucite matrix. Experiments indicate that the transition is not produced at all unless the peak stress in the mixture exceeds about 30 kbars and at high peak stress the transition occurs at about 25 kbars. These conclusions are not totally unreasonable, but they cannot be considered firm without additional experimental support.

Section V contains a list of nine papers, talks and reports produced under this contract.

TABLE OF CONTENTS

		Page
FOREWORD		iii
ABSTRACT		iv
LIST OF TABLES		ix
LIST OF FIGURES		x
PART I:	DYNAMIC FAILURE IN LiF	1
	A. Introduction	1
	B. Experimental Procedures	2
	C. Experimental Results	8
	D. Analysis	8
	E. Discussion	11
	1. Impurity Effect	13
	2. Multiplication Effects	13
	3. An Empirical Relation	16
	4. High Velocity Effects	16
	F. Future Plans	18
	References	21
	TABLES I through VIII	23
	Figures 1.1 through 1.5	32
PART II:	MULTIPLICATION OF DISLOCATIONS IN LiF	37
	A. Introduction	37
	B. Description of Apparatus	39
	C. Associated Instrumentation	40
	1. Projectile Velocity Measurements	40
	2. Measurement of Tilt	41
	3. Measurement of Stress Pulse Duration	41

Page

D. Sample Preparation 42

E. Polishing and Etch-Pit Analysis 43

F. Static Mechanical Deformation Behavior 44

G. Future Effort 45

References 47

Figures 2.1 through 2.5 48

PART III: WEAK SHOCK IMPEDANCE METHODS FOR THE QUARTZ GAUGE 53

A. Introduction 53

B. Elastic-Plastic Material of Higher Impedance than Quartz 54

C. Polymorphic Material with Impedance Higher than Quartz 56

D. Materials with Impedance Lower than Quartz 57

References 60

TABLE IX 61

Figures 3.1 through 3.6 62

PART IV: SHOCK COMPRESSION OF CdS 68

A. Introduction 68

B. Method of Mixtures 68

C. Target Preparation 70

D. Experimental Results 70

References 72

TABLES X and XI 73

Figures 4.1 through 4.4 75

Page

PART V: REPORTS, PUBLICATIONS AND PAPERS 79

LIST OF TABLES

Table		Page
	PART I: DYNAMIC FAILURE IN LiF	
I	Impurity Measurements	23
II	Hydroxide Ion Analyses	24
III	Impurity Concentrations	25
IV	Dislocation Densities	26
V	Yield Strengths	27
VI	Shock Data	28
VII	Fit to Precursor Data Using Gilman Model	30
VIII	The Empirical Relation	31
	PART II: MULTIPLICATION OF DISLOCATIONS IN LiF	
IX	Double Shock Wave in CdS	61
	PART III: WEAK SHOCK IMPEDANCE METHODS FOR THE QUARTZ GAUGE	
X	Data and Computations	73
XI	Data and Computations	74

LIST OF FIGURES

Figure		Page
	PART I	
1.1	Experimental arrangement for the impact studies	32
1.2	Elastic precursor amplitude as a function of propagation distance	33
1.3	Effects of varying N_{mo} and D in the Gilman Model	34
1.4	Drag stress required to fit precursor decay curves vs divalent impurity concentration	35
1.5	One parameter fit to decay data, Eq. (1.13)	36
	PART II	
2.1	Effect of tilt on inclination of shock front	48
2.2	General schematic of the impact apparatus	49
2.3	Schematic layout of impact region	50
2.4	Arrangement of LiF specimen at bottom of impact plate . .	51
2.5	Photo-sensing Velocity System	52
	PART III	
3.1	Typical shockwave experiment	62
3.2	P-u plane of elastic-plastic material of higher impedance than quartz	63
3.3	P-u plane of polymorphic material with a higher impedance than quartz	64
3.4	Flow of numerical impedance calculation for polymorphic material of higher impedance than quartz	65
3.5	P-u plane of material with a lower impedance than quartz .	66
3.6	Flow of numerical calculation for material of lower impedance than quartz	67

Figure		Page
	PART IV	
4.1	Typical target assembly	75
4.2	Wave profiles in CdS matrix	76
4.3	Pressure volume plots of shot 69-015 and 69-036	77
4.4	Pressure volume plots of shot 69-005	78

PRELIMINARY DATA

I. DYNAMIC FAILURE IN LiF

James Asay

A. INTRODUCTION

One of the active areas of theoretical research in shock wave effects relates to the relaxation properties of materials under high rates of loading. In this respect, there has been considerable effort to describe such effects in terms of the dynamical properties of dislocations. However, existing theoretical models are still speculative, since they have not been well substantiated by experiments at high strain-rates. Most of the previous experimental work on stress-relaxing solids has been confined to polycrystalline materials.[1.1-1.5] Comparison with theoretical models is complicated in these materials because of grain boundary effects and mechanical anisotropy within grains. However, in single crystals these effects are absent and the analysis of experimental results is easier. Consequently it has been established as the major objective of the present work to experimentally determine elastic precursor decay in LiF and to relate this to theoretical models.

Single crystal LiF was chosen for this study since its behavior under static loading is well known. Gilman and Johnston[1.6] have shown that the yield behavior of LiF at low stress and strain-rates can be explained in terms of a stress-activation model for dislocation mobility. In addition, they have extensively studied multiplication mechanisms for dislocations in LiF, so that the dislocation parameters are relatively well known.

In the present experiments, LiF was impacted on a {100} crystallographic plane at a stress of about 27 kbars. The decay of the elastic precursor was

then determined as a function of propagation distance. These data allow experimental determination of an attenuation function describing the decay of the elastic precursor with distance. This can be compared with theoretical predictions of decay to obtain information about rate-dependent behavior in LiF.

B. EXPERIMENTAL PROCEDURES

LiF studied in the present experiments was obtained from three different suppliers and six separate boules.

The first set of specimens, of X-ray monochromatic grade, was obtained from Semi-Elements, Inc.[a] The two different boules from which specimens were obtained will be referred to as materials II and IV. Specimens from both these materials were received in the form of flat plates with surfaces parallel to {100} crystallographic planes. Crystals from material II were prepared by sawing, whereas those from the other boule were cleaved. Both sets of crystals displayed a fairly high density of subgrain boundaries. In addition, Laue back-reflection experiments indicated that the angular misorientation between adjacent subgrains was as high as 2^{o}.

Two other sets of crystals of X-ray monochromatic grade received from Harshaw Chemical Co.[b] will be referred to as materials I and III. Both of these were received in the cleaved condition and with the previously stated crystallographic orientations. However, the Harshaw crystals exhibited better optical quality and a lower density of subgrain boundaries

---

[a]Semi-Elements, Inc., Saxonburg, Pa.

[b]Harshaw Chemical Co., Cleveland, Ohio

than those from Semi-Elements. The maximum misorientation between grains was less than $1/2^{o}$ for the Harshaw crystals.

Two additional "ultrapure" materials have been studied. The first was purchased from the University of Utah[a] and will be referred to as material V. The other was obtained from Harshaw Chemical Company as vacuum ultraviolet grade LiF. It represents their purest grade and will be referred to as material VI.

Table I lists average impurity levels for crystals I-IV used in the shock experiments. The metallic impurities listed in the table were determined by emission spectroscopy and are claimed to be accurate within ±50% of the amounts present.[b] To better characterize the specimens, infrared studies were performed on representative samples from boules I-IV. Table II indicates the relative OH ion content for each material as determined by these studies.[c]

Table III lists the impurity levels for all materials studied to date. As will be shown, the divalent impurity concentrations exert the greatest influence on decay. Only magnesium is reported in this table since it is the principal divalent impurity in the present experiment, and since other investigators usually report it as the principal impurity in static hardening experiments in LiF.

The total divalent impurity contribution was also determined by a conductivity technique. Briefly, the method consists of measuring the

---

[a] F. Rosenberger, Physics Department, University of Utah, Salt Lake City, Utah

[b] American Spectrographics Lab., San Francisco, California

[c] T. Stoebe, Metallurgy Department, University of Washington, Seattle, Washington.

temperature dependence of the conductivity in insulators.[1.7,1.8] In alkali halides conduction is governed by the mobility of cation and anion vacancies; and for each type of defect it can be represented as

$$\sigma = ne\mu$$
$$= (K/T)\exp(-E/kT) \qquad (1.1)$$

where n is the concentration of vacancies, μ is the corresponding mobility, e is electron charge, E is the energy of vacancy motion, k is Boltzmann's constant, K is a constant and T is absolute temperature.

The total conductivity at any temperature is thus given by the sum of two terms like Eq. (1.1). The basis of the technique relies upon the fact that the conduction at high temperatures is governed by both the anion and cation mobilities. However, at lower temperatures the conductivity is influenced mainly by the cation vacancies (since the cation mobility is larger than that due to anions).

From the conservation of charge, there is a correspondence between the number of anion vacancies and the anion impurities, and, similarly, between the cation impurities and vacancies. Hence, a determination of the total cation vacancy concentration allows a calculation of the divalent impurity concentration. Stoebe[1.7] has studied the conductivity of LiF for doping levels ranging from $\sim$1 ppm to 320 ppm of magnesium. An unknown material can then be analyzed by comparison with his standardized curves. He states that the determination of the absolute magnitude of the impurity concentration can be made to within ±50% with this technique, and that relative magnitudes can be made to about ±15%.

As shown in Table III the agreement between the total divalent impurity levels determined by spectrographic and conductivity methods is

fair, within the accuracy of both techniques (about ±50%). The one exception is material III. However, as indicated in Table II, this material is the only one that exhibited a large concentration of OH ions (about 120 ppm). Stoebe[1.7] has also studied the OH effect in conductivity analyses, and concludes that the OH ion complexes with a Mg^{++} ion and a cation vacancy. This lowers the mobility of the resulting complex so that effectively it doesn't contribute to the overall cation mobility at the lower temperatures. The resultant effect is to lower the apparent amount of divalent impurities, which is consistent with the discrepancy for material III.

As indicated in the table, the conductivity determined impurity content is usually larger than the magnesium content determined spectroscopically. This is expected since the total divalent impurity level will contain contributions from cations other than magnesium (which are not reported in the table).

An important parameter required in theoretical analyses is the mobile dislocation density. The total density was measured using standard etch pit methods[1.6] on most of the samples studied and the average results are reported in Table IV. About half of the dislocations observed were in low angle subgrain boundaries and half in the interiors of the subgrains. Because of sample-to-sample variations and the variations within a given specimen, the results are estimated reliable to only within a factor or two. Also shown in Table IV are independent measurements by T. G. Stoebe. As indicated, the agreement between the two investigations is fair, although values for materials I and III

determined here are generally lower. For later calculations, the arithmetic means reported in the table were used.

In order to provide a comparison with elastic precursor amplitudes, the static yield stresses were also determined for most of the specimens. These values were obtained by compression tests in an Instron machine[a] and the average results are reported in Table V. Most of the specimens used for these measurements had dimensions of approximately 1/4" x 1/4" x 1/2", although it was found that these dimensions are not critical. The uncertainty in the static yield strengths was estimated from sample-to-sample variations to be about 10%.

Samples I-IV were prepared for gas gun studies by lightly lapping to remove cleavage steps and then analyzing by the Laue method to check the orientation of crystallographic planes. A quartz gauge was bonded to a free surface and the entire assembly was cast with epoxy in a steel mounting ring. Prior to the shock experiment, the assembly was mounted at the end of the 4-inch gas gun previously described.[1,9]

The sample preparation for material VI was somewhat different from that previously used. Since this crystal is so soft (the flow stress is $\sim$0.017 kbars), it is supplied in the irradiated condition.[b] This allows cleavage without inducing internal damage. Furthermore, the initial condition can be restored by high temperature annealing. The size of the as-received crystal was $\sim$1" x 1-1/2" x 1-1/2". Square specimens with lateral dimensions of $\sim$3/4" x 3/4" x 4 mm thick were cleaved from this.

---

[a]The applied strain rates used were typically on the order of 5×10^{-4}/sec.

[b]The blank had initially been irradiated with a Co^{60} source to a total dose of $\sim 2 \times 10^6$ rads by the supplier. This treatment increased the flow stress to $\sim$0.24 kbars.

The specimens were then annealed at 600°C for 24 hours and oven cooled for 24 hours to room temperature. Some of the samples were then reirradiated to various doses of γ-rays from a Co^{60} source.

Figure 1.1 illustrates the experimental arrangement. The quartz transducer was used in the shorted condition with a 10-ohm resistance across the active center. Four shorting pins positioned around the specimen (not shown in the diagram) were used to measure the projectile tilt, which was usually on the order of 0.1 to 0.4 milliradians. The projectile velocity was determined to within 1/2% with four pins placed in front of the target assembly.[1.9]

Wave velocities were initially determined with techniques described earlier.[1.9] However, because of the relatively high elastic velocity in LiF and the thin specimens employed, variations of approximately 2 to 3% from the acoustic velocity were routinely observed. To improve the velocity measurements a technique was devised which allowed both higher precision and greater accuracy. Since LiF becomes polarized under shock conditions, an electrode was placed on the rear surface of the specimen to detect the polarization signal. Upon impact a fast-rising signal was observed on the electrode, which was then added to the quartz signal at the input terminals of a Tektronix 454 oscilloscope. Since time errors arise only because of differences in the cable lengths for transducer and polarization signals they can be easily determined, so that the wave transit time can be measured with high precision. On four specimens a maximum variation of about 1/3% was observed in the velocity, with the average being about 3/4% higher than the acoustic value of 6.57 mm/μsec.

As mentioned, the quartz gauge allows a determination of the stress-time profile at the specimen rear surface. These profiles consist of an elastic precursor with risetime on the order of 10 nsec or less, followed by a region of stress relaxation and finally by the plastic profile. For the impact stresses of 27 kbars employed in these experiments, it was found that the profiles are not steady in LiF. That is, the amplitude of the elastic precursor decreases with propagation distance and the risetime of the plastic wave increases approximately linearly with increasing propagation distance.

C. EXPERIMENTAL RESULTS

Table VI lists the results of all impact experiments performed on LiF, and the order in which they were performed. The elastic precursor amplitudes (HEL) reported in the table were calculated from the measured amplitudes in quartz by using the elastic transmission function for wave transmission at the LiF-quartz boundary. In terms of the longitudinal stress in the quartz, P_q, the stress in the specimen, P_s, is given as

$$P_s = (1.072)P_q.$$

Some of the samples were irradiated with γ-rays from a Co^{60} source; the purpose of this was to control the initial concentration of point defects.

All precursor amplitudes are plotted as a function of propagation distance in Fig. 1.2. The grouping of the data into separate curves representing each boule is clearly evident.

D. ANALYSIS

In relating present experimental results to theoretical calculations, different models of stress relaxation have been employed. Each of these

was used to obtain a functional relationship between the rate of decay of the elastic precursor and an attenuation function. The approach will be outlined as follows: The rate of decay of the elastic precursor, dP_x^e/dt, is related to an attenuation function, $F(\rho,P_x^e)$, as

$$dP_x^e/dt = -F(\rho,P_x^e)/2 \tag{1.2}$$

When a form for F is chosen, material properties or empirical parameters can be used to obtain a theoretical prediction of the elastic precursor decay through the use of Eq. (1.2). The theoretical decay curve can then be compared with experiment to test the validity of the model.

Duvall[1.4] assumed a simple relaxation model to fit precursor decay in Sioux quartzite. If P_x^s is the equilibrium Hugoniot stress corresponding to some value of particle velocity and P_x^e is the corresponding value of the elastic precursor, then a possible relation between F and stress can be expressed as

$$F(\rho,P_x^e) = (P_x^e - P_x^s)/T \tag{1.3}$$

where T is a relaxation time. This function results in a stressed element relaxing exponentially toward a state of static compression. The quantity T is characteristic of the decay and may be related to the strain-rate for plastic deformation or represent fracture time for brittle fracture.[1.4] For the experimental data represented in Fig. 1.2, the relaxation time varies from 0.015 μsec to 0.085 μsec. However, the relation doesn't agree with experiments very well, since the data do not follow a simple exponential dependence upon stress.

Another model of stress relaxation which has received considerable recent attention was proposed by Gilman[1.6] to explain static yielding in

terms of dislocation processes. It is based upon a stress-activated model of dislocation glide, which is applicable in a variety of metals and ionic crystals at low stress and strain-rate levels. Gilman shows that the plastic strain-rate along a glide plane is given as the product of the Burgers vector, the mobile dislocation density, and the dislocation velocity. In his model the dislocation velocity is given in terms of the applied shear stress τ as

$$v(\tau) = v_o\, e^{-D/\tau} \tag{1.4}$$

where v_o is usually taken as the shear velocity; in this case:

$$v_o = \sqrt{(C_{11} - C_{12})/2\rho_o}$$

D is a drag stress which inhibits dislocation glide.

In applying this model it is necessary to know the applied shear stress on a dislocation and the active slip planes. In LiF, there are six primary <110>{110} slip systems. For propagation along the [100] direction, as in the present experiments, four of these are active. With Gilman's relation (1.4) for the dislocation velocity, Johnson et al.[1.10] show that the precursor decay rate in LiF can be expressed as

$$dP_x^e/dt = -(C_{11} - C_{12})bN_{mo}v(\tau)/6 \tag{1.5}$$

where C_{11} and C_{12} are elastic constants, b is the Burgers vector, N_{mo} is the initial mobile dislocation density, and τ, the resolved shear stress, is

$$\tau = P_x^e(C_{11} - C_{12})/2C_{11} \tag{1.6}$$

The present data can then be compared with theoretical predictions based on independently determined dislocation parameters. Figure 1.3

illustrates a comparison between Gilman's theory as given in Eq. (1.5) and the experimental data corresponding to curve 1 of Fig. 1.2. Curve A was obtained by using the measured dislocation densities of Table IV as an upper limit to the mobile density and Gilman's[1.6] value of 1.69 kbars for the drag coefficient. However, the agreement is poor. Curve C illustrates the effect of increasing the dislocation density so as to best fit the experimental data. For this curve D was held constant and the density was increased to $1 \times 10^7/cm^2$. However, the best fit to the experimental data is obtained by varying both the parameters. Curve B corresponds to an initial density of $5 \times 10^8/cm^2$ and a drag stress of 20 kbars. Both these values are beyond any uncertainties in their determination. In particular, the dislocation density is at least three to four orders of magnitude higher than that determined experimentally.

The parameters D and N_{mo} were adjusted for each material to best fit the data. The resulting fits are shown in Fig. 1.2 and values of D and N_{mo} are reported in Table VII.

E. DISCUSSION

Gilman[1.11] has shown that some of the dislocations in LiF are not pinned by defects, and he refers to these as mobile dislocations. The etch technique used here did not distinguish between the initial mobile and pinned contributions to the density. Although the distinction is important in some dislocation experiments, it may not be applicable in the present experiment. Under the high shear stress developed in the shock (up to 7.8 kbars at the impact surface), it is reasonable to assume that many dislocations will become mobile. For the pinning point separations typical of the specimens employed here, the dislocation should break away from the

defects at a maximum shear stress of about 0.5 kbars. Hence, for practical purposes the measured densities should represent the mobile densities.

In addition, Gilman[1.11] has demonstrated a one-to-one correspondence between the etch pit technique and the true dislocation density in LiF. Therefore, the values reported in Table IV should be taken as the initial densities. However, these are in major disagreement with the required values reported in Table VII. Furthermore, the drag parameter reported in the literature typically ranges from about 0.2 kbar for high purity LiF[1.12] to about 2 kbars for less pure specimens.[1.11] These values are in complete disagreement with the range of ∿5 to 12 kbars reported in Table VII.

The discrepancy in D will be considered first. Since the mean pressure at the elastic front is

$$\bar{P}^{e} = (P_x^{e} + 2P_y^{e})/3$$

$$= P_x^{e}(C_{11} + 2C_{12})/3C_{11} \qquad (1.7)$$

it is possible that the increase in the drag parameter could result from a strong hydrostatic pressure dependence. Hanafee[1.12] observed that this parameter does increase approximately linearly with hydrostatic pressure in LiF. However, the effect of this is to multiply the factor v_o in Eq. (1.4) by a quantity somewhat less than 1. If D' is the pressure derivative of the drag stress and D_o is the atmospheric value, the velocity dependence becomes

$$v = v_o \exp[-(D_o + D'\bar{P}^{e})/\tau]$$

$$= v_o' \exp(-D_o/\tau) \qquad (1.8)$$

since τ can be related to $\bar{P}^{e}$ at the elastic front. Thus, Eq. (1.8) implies

that the atmospheric value of the drag stress should still control the dislocation mobility in precursor studies. However, as implied by Eqs. (1.4), (1.5) and (1.8), the apparent values of the dislocation densities may vary from the measured values (if the shear velocity is used for v_0), due only to the hydrostatic pressure dependence of the mobility.

1. Impurity Effect

Before discussing the reasons for the discrepancies in the actual mangitudes of D and N, the Gilman model can be partially tested. Gilman has shown that the activation energy for dislocation motion varies as the square root of the divalent impurity concentration for moderate dislocation velocities. The result of this is to replace the drag stress D_0 in Eq. (1.8) by the quantity

$$D_0 = A(T)C^{1/2} \tag{1.9}$$

where A(T) is a constant at a given temperature and C is the defect concentration. Since this equation is directly related to Gilman's derivation of Eq. (1.4), it allows another test of his theory.

Figure 1.4 is a graph of the drag stress required to fit the decay curves as a function of the divalent impurity concentration. Within the accuracy of the impurity measurements, the square root dependence is approximately verified. The one exception is the data point in parenthesis. However, as previously noted, this material contains OH ions, which may influence the interaction.

2. Multiplication Effects

Although Gilman's theory appears to predict the correct dependence of the decay rates upon defect concentration, there is still a

discrepancy between the actual magnitudes for N and D required in the theory. It is evident from the discrepancy in the dislocation density that if any model of dislocation glide is applicable, then the effective density at the wavefront must be increased by three to four orders of magnitude.

Multiplication mechanisms are not currently known very well, particularly for the stress range employed here. Some recovery experiments on MgO shocked to 80 kbars suggested that the dislocation density increased about 25 times over that in crystals deformed by slow compression to the same plastic strain.[1.13] These experiments also indicated that slip occurred prior to fracture, which indicates that fracture at the elastic front is not responsible for precursor decay in MgO. Since the slip system in MgO is similar to that for LiF this lends support to the possibility that dislocation glide controls precursor decay in the present experiments.

Of the various multiplication mechanisms which can increase the dislocation density, only the Koehler cross-glide model is fast enough to give the large increases necessary in the present experiments (unless dislocations are spontaneously nucleated at the front). For crystal orientation similar to that studied here, Gilman[1.14] has determined the rate of multiplication as a function of the applied shear stress on the primary slip systems in LiF. By applying stress pulses of known duration and measuring the subsequent change in dislocation density, he has found that the rate of multiplication can be expressed as

$$dN/dt = c_0 e^{-B/\tau} v(\tau) N \qquad (1.10)$$

where c_0 is a constant, B is a drag parameter relating to glide on the cross slip plane, $v(\tau)$ is the dislocation velocity on the primary slip system and N is the instantaneous dislocation density.

Characteristic theory can be modified to give an approximate description of multiplication at the wavefront as follows. If spontaneous nucleation does not occur, the density can be approximated as a Taylor expansion around the wavefront, having risetime Δt, as follows:

$$N(P_x,t) = N_o + (\partial N/\partial t)_{p_x,t_o} \Delta t + \ldots$$

$$\approx N_o + (\partial N/\partial t)_{p_x,t_o} \Delta t \qquad (1.11)$$

Using Eqs. (1.10) and (1.11) and assuming that the second term above is the dominanat one, Eq. (1.5) can be written as

$$\frac{dP_x^e}{dt} \approx - \left(\frac{C_{11} - C_{12}}{6}\right) bc_o N_o \Delta t e^{-B/\tau} v^2 \qquad (1.12)$$

Although Gilman's data are rather limited and the purity of his crystals is unknown, the data will allow a rough estimate of multiplication. The experimental values of c_o and B in Eq. (1.10) are

$$c_o = 8.5 \times 10^5/\text{cm}$$

$$B = 3 \text{ kbars}$$

Using Gilman's [1.11] value of 1.7 kbars for the drag stress D_o in "impure" LiF, the quantity $e^{-B/\tau} v^2$ becomes $v_o^2 \exp(-6.4/\tau)$. The value of 6.4 kbars is in good agreement with the value of 6 kbars used for curve III in Fig. 1.2. If the multiplication time, Δt, is now adjusted to give the correct pre-exponential factor in Eq. (1.12), a value of 3 nsec is obtained. This is well within the measured risetime of the elastic wave (about 10 nsec).

The above calculation indicates that both the required dislocation densities and the high values for the drag stress required to fit the data

are plausible, if sufficient multiplication occurs at the elastic front. However, the calculation is somewhat speculative, since multiplication data are not available for a variety of specimen purities and over large stress ranges. In this respect, the multiplication work which is currently in progress at WSU should help resolve this question.[a]

3. An Empirical Relation

An empirical relation of the form

$$dP_x^e/dt = -K(P_x^e - 2)^2 \qquad (1.13)$$

fits the data as well as Gilman's model. Figure 1.5 shows the curves predicted from Eq. (1.13), and Table VIII reports values of K for the various curves. Using Mason's[1.15] assumption that the dislocation velocity varies linearly with stress at the higher stress levels and Eqs. (1.10) and (1.11), the form of this equation can be justified. Also, the equilibrium value of 2 kbars in Eq. (1.13) can be explained from Gilman's experimental determination that the dislocation velocity in impure LiF rapidly approaches zero with decreasing stress for a shear stress of about .7 kbars ($P_x^e \sim 2.5$ kbars).

4. High Velocity Effects

Gilman[1.16] states that his model may not be valid for dislocation velocities near the sound velocity and implies that other effects such as

---

[a] Klein's experiments on MgO indicate that cross glide may be possible for propagation along the [100] direction in rocksalt structure. However, his results are somewhat inconclusive, since the slip-band geometry in the shocked MgO changed from fine edge bands near the impact surface to broad screw dislocation bands further into the samples. This could be due to pulse spreading, to edge effects, or to changes in the loss mechanism as the precursor amplitude changes.

dislocation acceleration, phonon scattering, or phonon viscosity may be predominant at these velocities. Two additional loss mechanisms have been studied in the present experiment. For the first calculation, Eq. (1.5) was expressed in terms of the plastic work done at the wavefront as

$$dP_x^e/dt = - (1/2)(C_{11}/P_x^e)(dW_{irr}/dt) \qquad (1.14)$$

One source of energy loss is due to the radiation of sound waves as a dislocation core expands and contracts over the potential hills in the lattice. For this situation, Nabarro[1.17] shows that the power required to maintain an average dislocation velocity is proportional to the cube of the velocity (for linear damping this implies that the loss is proportional to $\tau^{3/2}$). As shown in Eq. (1.14), this results in a decay rate proportional to the square root of the stress. Although this mechanism can cause large energy losses, the predicted stress dependence disagrees with the observed dependence. This implies that this type of loss should not predominate in the present example.

Another loss mechanism which has been proposed relates to the interaction of a dislocation with the phonon gas in the lattice. Mason[1.15] has shown theoretically that the steady state dislocation velocity in this model varies linearly with stress and has obtained damping constants which are in good agreement with acoustic experiments. However, the model predicts that impurities influence the motion only by controlling the breakaway stress of the dislocation from the impurity. As illustrated in Figs. 1.2 and 1.5 this contradicts the present experimental data.

Other high velocity loss mechanisms are currently being studied with respect to their applicability in the present case.

F. FUTURE PLANS

As is well known, the flow stresses at low strain-rates can be explained in terms of the interaction of point defects with dislocations. In general, the strength of pinning by point defects is a strong function of the type of defect. Fleischer[1.18, 1.19] has shown that impurities which cause symmetrical strain distortions in the lattice (e.g. monovalent substitional atoms in LiF) interact only with the dilatational fields of edge dislocations and usually produce a small amount of hardening per defect. He also shows that those defects which produce non-symmetrical distortions (e.g. divalent atom-vacancy complexes) can interact with both edge and screw dislocations and generally cause a high degree of hardening per defect.

Since the present experimental results for the static yield strengths agree with his theory and since the precursor curves suggest a strong dependence upon divalent impurities, it would be important to establish the correlation between the two cases. In particular, if Gilman's prediction for dislocation mobility (Eq. (1.9)) were valid for the precursor curves, it would suggest further that dislocation glide is actually responsible for the decay. In addition, these experiments would allow an estimation of how impurities interact with dislocations at high velocities.

As illustrated in Fig. 1.4, Gilman's prediction of the drag stress versus impurity concentration does seem to be valid in the present case. However, there are a number of complications in the present experiment which make the comparison dubious. These are:

1) Some of the observed differences might be caused by possible differences in dislocation densities.

2) The effect that OH ions have on precursor decay is unknown, so that material III cannot be used with confidence in this comparison.

3) It is difficult to reliably control the impurity content in order to systematically study the effect.

4) Although the current data imply that divalent ions are responsible for the decay, it is possible that some unknown parameter causes the observed variations.

The elastic distortions produced by divalent atom-vacancy complexes (usually referred to as elastic dipoles) are also produced by interstitial atom-vacancy complexes. These defects can be induced by irradiation with neutrons, electrons, or γ-rays. Thus, a means exists whereby the impurity effects previously observed can be studied in a systematic way. In addition, most of the above uncertainties can be eliminated, since the dislocation density remains constant under γ-irradiation and other material properties should remain unchanged.

In view of these considerations, a set of experiments has been planned to measure the dynamic yield stress in specimens irradiated with different doses of γ-irradiation from a Co^{60} source. As indicated in Table VI, experiments have been started and to date have qualitatively confirmed expectations based upon the above arguments. Additional experiments are planned for dose rates ranging from $\sim 5 \times 10^7$ to 1×10^8 RADS (to simulate curves II and III of Fig. 1.2).

The main objective of these experiments will be to test the mobility relation given in Eq. (1.9). As mentioned, this information will allow a test of Gilman's relation (or other dislocation models), independently of

whether multiplication occurs at the wavefront (as suggested by the discrepancies in N and D). Also, the data will allow estimations of point-defect-dislocation interactions at stresses and strain-rates which have not been previously obtained.

In addition to the above experiments, the following shots are planned to further confirm the decay curve in material III.

1) Fig. 1.2 suggests that the decay curve may have a discontinuous break at about 6 kbars. This could result from the possibility that the decay may not be determined by a single mechanism over the whole range of stress. For this reason, four shots are planned to determine if there is a break in the curve and to determine the asymptotic value of stress for large propagation distances.

2) One shot to directly determine the impact stress. Because of the fast response of quartz, this experiment should help indicate whether significant stress relaxation occurs during the application of stress.

REFERENCES

1.1. J. W. Taylor and M. H. Rice, J. Appl. Phys. 34, 364 (1963).

1.2. T. J. Ahrens and G. E. Duvall, J. Geophys. Res. 71, 4349 (1966).

1.3. R. W. Rohde, Acta Met. 17, 353 (1969).

1.4. G. E. Duvall, "Propagation of Plane Shock Waves in a Stress Relaxing Medium," in STRESS WAVES IN ANELASTIC SOLIDS, H. Kolsky, Ed. (1964).

1.5. J. M. Kelly and P. P. Gillis, J. Appl. Phys. 38, 4044 (1967).

1.6. J. J. Gilman and W. G. Johnston, DISLOCATIONS AND MECHANICAL PROPERTIES OF CRYSTALS, J. G. Fisher, Ed.

1.7. T. G. Stoebe and P. L. Pratt, Proc. Brit. Ceramic Soc. 9, 181 (1967).

1.8. T. G. Stoebe, J. Phys. Chem. Sol. 28, 1375 (1967).

1.9. G. R. Fowles, G. E. Duvall, J. Asay, P. Bellamy, F. Feistmann, D. Grady, T. Michaels and R. Mitchell, Washington State University Report WSU SDL 69-02 (1969).

1.10 J. N. Johnson, O. E. Jones and T. M. Michaels, J. Appl. Phys., 41, 2330, (1970).

1.11 J. J. Gilman and W. G. Johnston, Solid State Physics 13, 147 (1962).

1.12 J. E. Hanafee and S. V. Radcliffe, J. Appl. Phys. 38, 4284 (1967).

1.13 M. J. Klein, Phil. Mag. 12, 735 (1965).

1.14 J. J. Gilman, J. Appl. Phys. 33, 2703 (1962).

1.15 W. P. Mason, "Dislocation Drag Mechanisms and Their Effects on Dislocation Velocities," in DISLOCATION DYNAMICS, p. 487, A. R. Rosenfield, G. T. Hahn, A. L. Bement and R. I. Jaffe, Eds., McGraw-Hill (1968).

1.16 J. J. Gilman, J. Appl. Phys. 36, 3195 (1965)

1.17 F. R. N. Nabarro, THEORY OF CRYSTAL DISLOCATIONS, Oxford University Press (1967).

1.18 R. L. Fleischer, Acta Met. 10, 835 (1962).

1.19 R. L. Fleischer, J. Appl. Phys. 33, 3504 (1962).

PRELIMINARY DATA

TABLE I

IMPURITY MEASUREMENTS

Material[b]	Impurity, ppm[a]							
	Si	Mg	Mn	Fe	Al	Cu	Ca	Cr
I (3)	30 - 80	100	---[c]	7 - 25	40 - 150	<5	<5	<.1
II (4)	50 - 150	100 - 150	<10	9 - 40	200	<5	5 - 10	<.1
III (10)	25 - 150	150 - 400	---	20 - 60	100 - 150	5 - 8	5 - 7	<.1
IV (3)	40	20 - 60	5 - 20	20 - 25	200	<5	<5	.2
V (2)	150	5 - 15	---	7 - 20	170 - 250	.1 - 5	4 - 5	.3
VI (3)	10 - 20	8 - 10	---	8 - 20	4 - 6	<1	1	<.1

[a]When more than one measurement was made as indicated by the numbers in parenthesis, the range is reported. The reported amounts were obtained by both American Spectrographic Co. and WSU College of Engineering.

[b]Materials I and III were obtained from Harshaw Chemical Co. Materials II and IV were obtained from Semi-Elements.

[c]The Harshaw crystals showed no detectable traces of Mn.

TABLE II

HYDROXIDE ION ANALYSES

Material	[a]Absorption, % 2.79 μ	2.80 μ	[b]Amount of OH ppm
I (1)	----[c]	----	< 5
II (3)	----	----	< 5
III (5)	20	55	120
IV (2)	----	----	< 5

[a]The infrared analyses were obtained with a Perkin-Elmer 225 spectrometer. The number in parenthesis indicates the number of crystals representing the reported amounts.

[b]The amounts reported here were referenced to a standard crystal containing 200 ppm of OH, and should be accurate to within a factor of 2.

[c]The absorption peaks for materials I, II and IV could not be differentiated from background. The reported amounts were determined from the maximum deviation of the baselines.

TABLE III

IMPURITY CONCENTRATIONS

Material	Spectrographic[a] ppm Magnesium	Conductivity[b] ppm
I	100 (3)	210 (1)
II	113 (4)	270 (1)
III	250 (9)	83 (1)
IV	40 (3)	83 (1)
V	10 (2)	25 (1)
VI	9 (3)	c

a. The numbers in parenthesis represent the number of measurements made to obtain the averages.

b. Total divalent impurity content determined by T. G. Stoebe, University of Washington, Seattle. In general this should be slightly larger than the Mg^{++} content.

c. Not completed.

TABLE IV

DISLOCATION DENSITIES

Material	Asay $\times 10^{-5}/cm^2$	Stoebe $\times 10^{-5}/cm^2$	Average $\times 10^{-5}/cm^2$
I	.5 - 1	4.1 (1)	2
II	5 - 10	3.9 (1)	5
III	.2 - 1	3.5-5.4 (3)	2
IV	5 - 30	3.2 (1)	6
V	1 - 3	1.2 (1)	2
VI	.25 $\pm$ .05 (10)	---[a]	

a. Not completed.

TABLE V

YIELD STRENGTHS

Material	Yield Stress[a] kbars	
I	0.32	(4)
II	0.32	(4)
III	0.43	(4)
IV	0.16	(5)
V	0.017	
VI	0.07	

[a]Numbers in parenthesis refer to the number of measurements representing this average.

TABLE VI

SHOCK DATA

Shot No.	Sample No.	Thickness mm	Proj. Vel. mm/μsec	Proj. Tilt milliradians	HEL kbars	Elastic Vel. mm/μsec
69-002	IV-1	15.440	0.342	---	1.9	----
69-006	IV-2	1.054	0.340	0.3	2.2	----
69-006	IV-3	1.823	"	0.3	3.6	6.31
69-008	II-1	3.205	0.346	0.1	13.2	6.51
69-011	II-2	2.113	0.335	<0.1	15.5	6.42
69-011	IV-4	2.273	"	"	4.5	6.14
69-016	IV-5[c]	2.159	0.331	0.1	3.1	6.10
69-016	II-3[c]	2.176	"	"	15.0	6.23
69-019	I-1	2.530	0.347	0.6[b]	15.8	6.33
69-019	I-2	2.290	"	<0.1	16.9	6.81
69-023	I-3	1.011	0.337	0.4	20.3	----
69-023	I-4	3.567	"	"	14.1	6.62[a]
69-039	I-5	0.345	0.336	0.2	18.5	----
69-039	III-1	4.065	"	"	5.2	6.63[a]
69-040	III-2	0.820	0.341	0.2	15.0	----
69-040	III-3	5.892	"	"	4.3	6.64[a]
69-041	III-4	2.365	0.333	0.4	10.5	----
69-041	III-5	7.880	"	"	3.7	6.62[a]

a. Elastic velocity obtained with polarization technique.

b. This sample was cleaved and mounted in a lapped ring without further lapping. It had a built-in tilt of about .6 milliradians.

c. Annealed at 600°C for 8 hours after final lapping.

TABLE VI Cont'd

SHOCK DATA

Shot No.	Sample No.	Thickness mm	Proj. Vel. mm/μsec	Proj. Tilt milliradians	HEL Kbars	Elastic Vel. mm/μsec
70-007	III-6[a]	1.078	0.340	0.3	16.0	----
70-007	III-7[a]	1.846	0.340	0.3	11.1	----
70-008	V-2[a]	1.038	0.346	0.1	3.6	----
70-008	V-3[a]	4.055	0.346	0.1	2.7	6.74
70-009	V-1A[b]	2.215	0.338	0.3	4.50	6.63
70-009	V-1B[c]	2.270	0.338	0.3	5.05	6.68
70-015	VI-3A	1.302	0.338	0.4	6.46	6.58
70-015	VI-3B	4.545	0.338	0.4	4.26	6.65
70-016	VI-1B[a,d]	1.431	0.336	0.2	3.26	6.60
70-016	VI-1C[a,d]	4.696	0.336	0.2	2.72	----

a. Annealed at 600°C for 24 hours.

b. Irradiated to a total dose of 5.5×10^6 RAD (Co^{60} source).

c. Irradiated to a total dose of 2.0×10^7 RAD (Co^{60} source).

d. Irradiated to a total dose of 6.5×10^6 RAD (Co^{60} source).

TABLE VII

FIT TO PRECURSOR DATA USING GILMAN MODEL[a]

Material	N_{mo} x 10^{-8}	D Kbars
I	2.0	12.0
II	2.0	10.5
III	2.0	6.0
IV	5.0	5.0
V	11.0	5.0
VI	11.0	5.0

a. The initial impact stress was taken to be 27 kbars.

TABLE VIII

THE EMPIRICAL RELATION[a]

Material	K, $(\text{Kbar-}\mu\text{sec})^{-1}$
I	0.082
II	0.109
III	0.28
IV	2.18
V	2.50
VI	2.50

a. $\frac{dP_x^e}{dt} = -K(P_x^e - 2)^2$

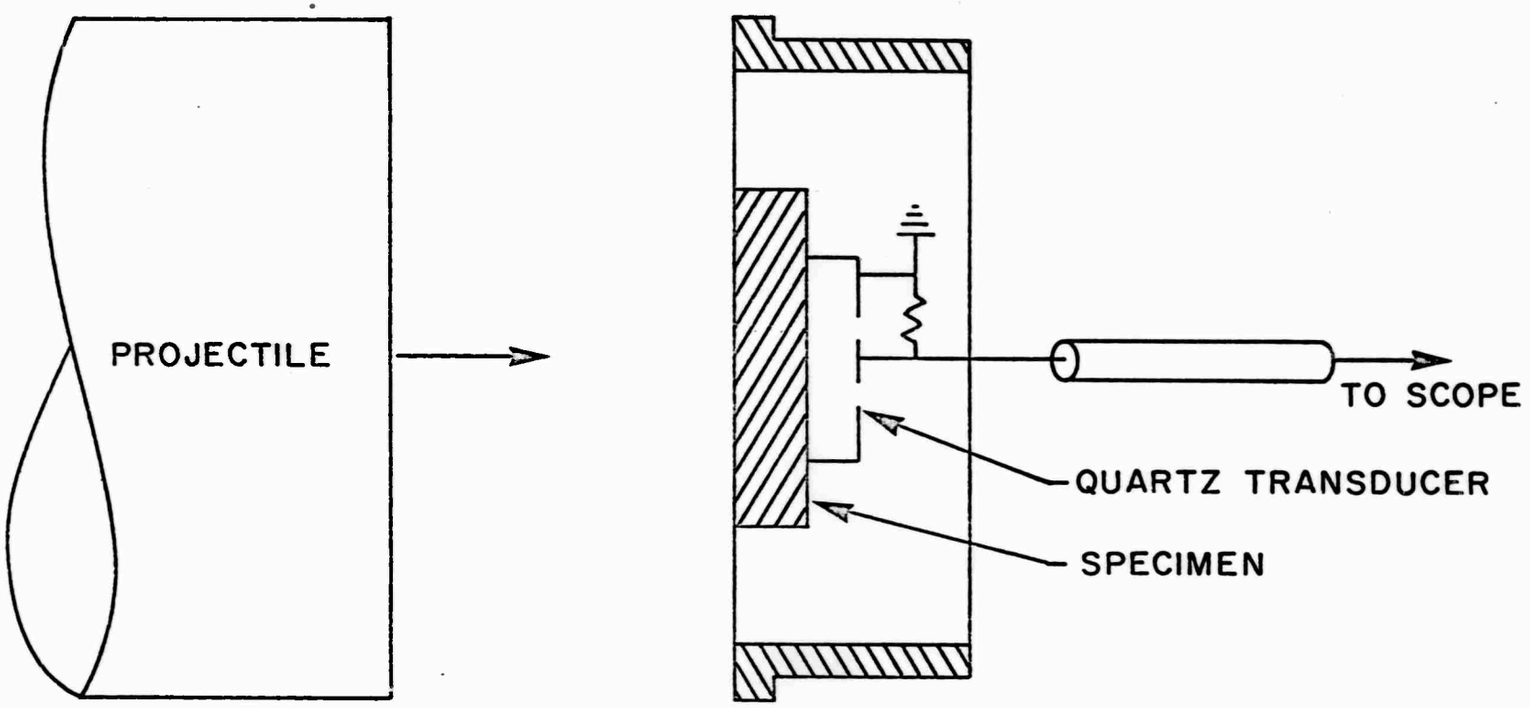

Figure 1.1 Experimental arrangement for the impact studies.

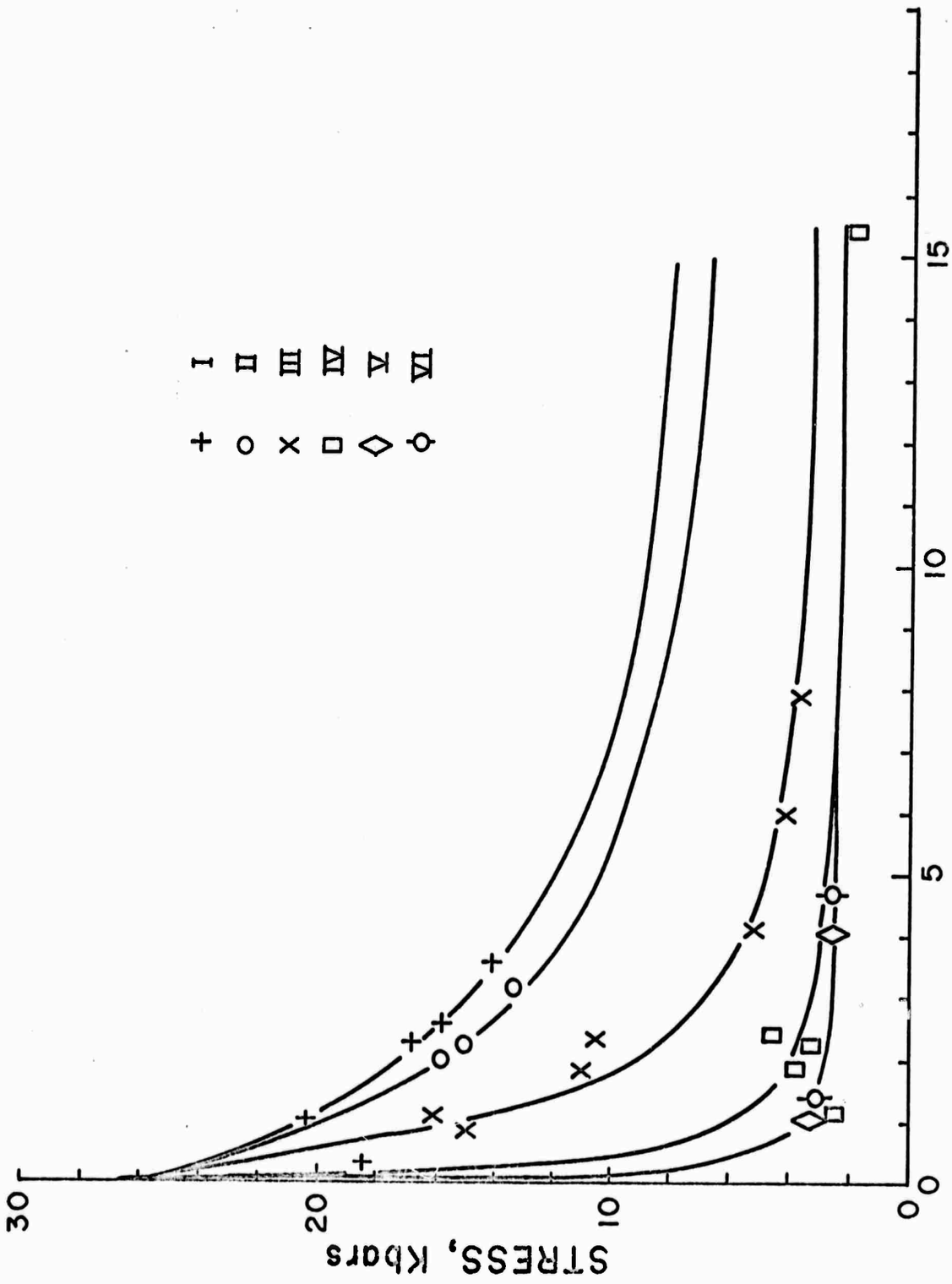

Figure 1.2 Elastic precursor amplitude as a function of propagation distance.

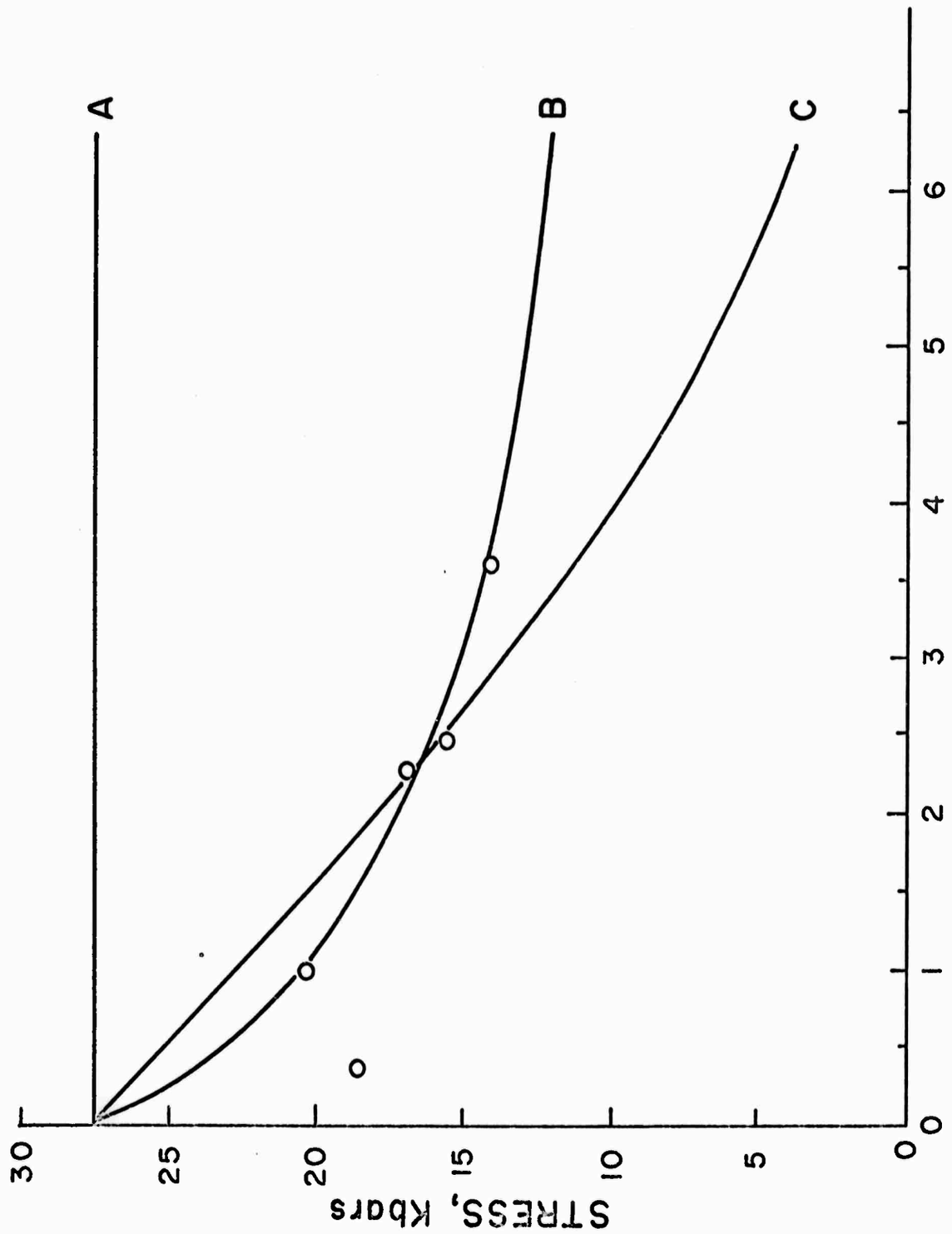

Figure 1.3 Effects of varying N_{mo} and D in the Gilman Model

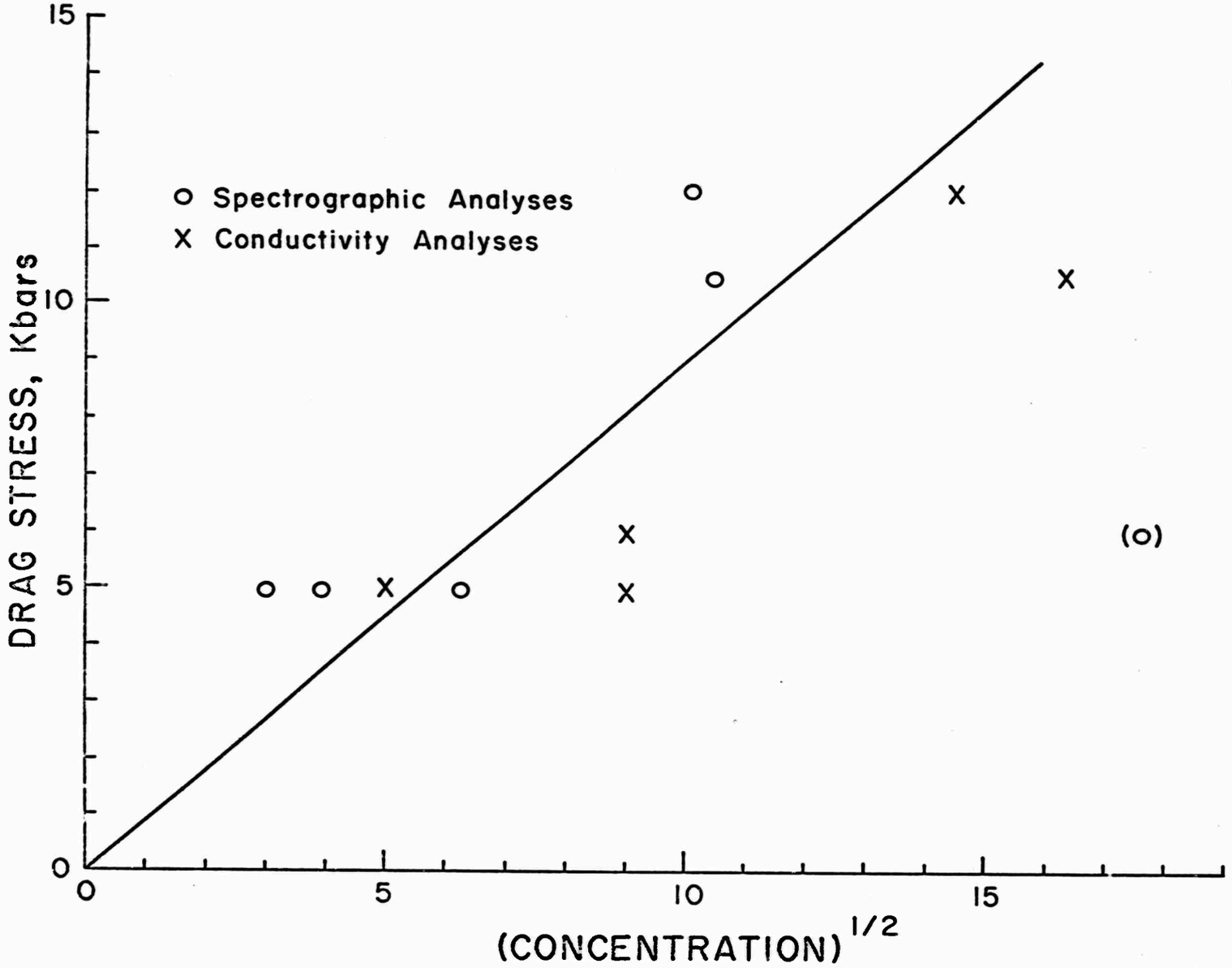

Figure 1.4 Drag stress required to fit precursor decay curves vs divalent impurity concentration

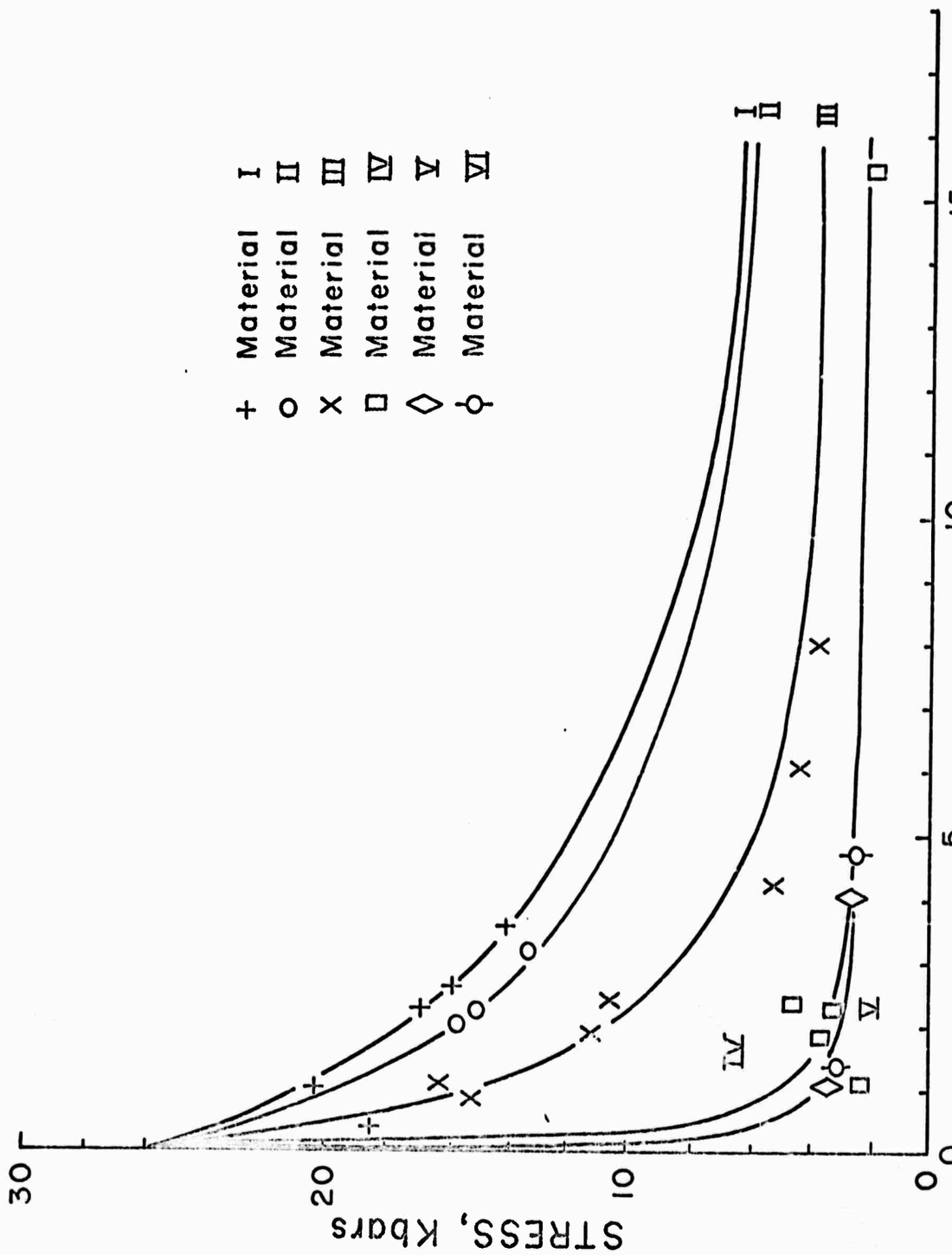

Figure 1.5 One parameter fit to decay data, Eq. (1.13)

II. MULTIPLICATION OF DISLOCATIONS IN LiF

J. E. Flinn

A. INTRODUCTION

Gilman has proposed and substantiated by extensive measurements at low strain-rates a cross-glide mechanism for multiplication of dislocations in LiF.[2.1] The theory predicts that dislocation density will increase after application of stress according to the relation

$$\rho(t) = M\rho_0 \exp(Mb\bar{v}t)/[M + \phi\rho_0\{\exp(Mb\bar{v}t) - 1\}]$$

where ρ_0 is initial density, M and ϕ are constants of the material and b and $\bar{v}$ have their usual meanings. Test of this relation requires application of rather small stresses with very high rates of loading for very short times. Bending and bar-on-bar impacts produce complicated and practically unanalyzable stress systems. Impact to produce weak plane shock waves and uniaxial strain naturally suggests itself, but a number of rather formidable difficulties arise because impact velocities must be very small.

What we would like to do is to apply discontinuously to the surface of a thin wafer a pressure of the desired magnitude, hold it for the required time, then release it discontinuously so that each volume element of the sample is stressed the required amount for a known time. These requirements rather closely dictate the apparatus design; and because of mechanical limitations, some compromise must be made in the definition of acceptable loading.

First of all, the threshold stress for multiplication in LiF is the order of a hundred bars. Application of a step in pressure implies shock

production by impact, and there are three conventional ways of producing plane shocks in the laboratory: by explosives, by impact of a solid projectile from a gun, by impact of a gas shock at the end of the shock tube. The first two methods produce shocks that are too strong; the last produces shocks that are too weak, besides producing very high temperatures at the surface of the sample. Of these three, projectile impact seems most promising of modification. The required stress implies impact velocity the order of a hundred cm/sec if solid projectile is to strike a solid target. This is too low for reliable gas acceleration but is within the reach of acceleration by gravity. So a drop apparatus has been designed and constructed.

It turns out to be impossible to achieve perfect planarity in a shock wave produced by any means. When a plane-faced projectile strikes the plane surface of a target, there is always some misalignment, and the acute angle between the two surface normals is called the "tilt" at impact. If the tilt is very small, the line of contact between the two impacting planes sweeps across projectile and target at supersonic velocity, inducing a shock wave in the target, as shown in Fig. 2.1. The inclination of the induced shock front with respect to the plane target surface is magnified by the ratio of projectile to shock velocities:

$$\text{Sin } \beta = (U_s/V_p) \sin \phi$$

If $\beta \geq 90°$, no shock is produced; the edge of the projectile thumps down on the target and eventually rolls over into a flat position in a rigid body-type motion. For V_p = 100 cm/sec and $U_s = 6 \times 10^5$ cm/sec, sin β = 1 when $\phi = 1.67 \times 10^{-4}$ radians. Tilt must be less than this in order that any shock at all be produced. It must be much less if the induced shock front is to be nearly parallel to the target surface.

Duration of plane shock impact on a sample can be controlled in two ways: duration of the applied pressure can be controlled, or pressure can be applied from a high impedance source so that the sample separates itself from the source after the induced wave has made a round trip through the sample and back to the source. The latter method is somewhat simpler in execution and was chosen for this problem.

B. DESCRIPTION OF APPARATUS

The apparatus must accelerate a projectile to the desired velocity, cause the flat face of the projectile to strike a flat plate in a planar impact, expose samples on the back face of the plate to the impact-induced shock wave for a specified time, and expel and preserve the specimen after it has been shocked. These requirements translate into control and measurement of four parameters: projectile velocity, tilt of projectile on impact, stress amplitude, stress duration.

A general layout is shown in Fig. 2.2. The apparatus is mounted on the wall as a single unit. Ample adjustment capability is provided for horizontal and vertical alignment. The impact arrangement consists of two projectiles, one rather loosely guided by an aluminum tube and the other closely guided by an air-bearing sleeve. The air-bearing sleeve serves two functions in that it greatly restricts lateral movement and provides nearly frictionless passage for the projectile. The projectiles will be classified as secondary and primary, respectively. Not shown in Fig. 2.2 is a small pressure tank, controlled by a solenoid valve which can be quickly emptied to provide additional acceleration to the falling secondary projectile. This projectile strikes the primary in turn and gives up a substantial portion of its momentum. In operation, the secondary projectile

is released and comes in contact with a trigger lever near the end of its fall. This lever holds the primary projectile at various heights (1.0 to 10 cm) above the impact plate. When triggered, the primary projectile begins its fall, but is soon struck by the secondary projectile.

The primary projectile has two parts - a thick (∿4 cm) nose cap and the main body (∿15 cm long). The nose cap screws onto the main body. Three caps have been made from nylon, aluminum and tool steel. With anticipated projectile velocities these provide a stress range from 0.025 to 0.75 kb. in the impact plate. The impact plate is made from an impact resistant tool steel. The alignment of the plate with respect to the primary projectile is done with three differential screws. This arrangement along with some auxiliary attachments necessary for parametric measurements is shown in Fig. 2.3.

The LiF specimen is in intimate contact with the bottom center of the impact plate as shown in Fig. 2.4. It is surrounded by aluminum plates which serve as momentum traps to prevent tensile waves running in from the lateral boundaries. In operation the shock wave passes from the impact plate into the specimen, traverses it, and reflects as a rarefaction from its face surface. When the rarefaction reaches the interface, tension is produced and the specimen separates from impact plate in a stress-free condition.

C. ASSOCIATED INSTRUMENTATION

1. Projectile Velocity Measurements

The system for projectile velocity and acceleration determination consists of three photo-transistors actuated by collimated light beams, with electronic circuitry for detecting each beam's closure by the falling

projectile. A general schematic illustrating the major features of the circuit is shown in Fig. 2.5. Included in the figure are representations of waveforms after each state. The NAND Gate produces three pulses, one for the closure of the beam to each photo-transistor. The time separation of pulses coupled with accurate measures of separations between collimated slits provides means of determining the projectile's velocity and acceleration near impact.

2. Measurement of Tilt

After preliminary adjustment has reduced the tilt to the order of 10^{-4} inches, final adjustment will be made by measuring the tilt of the shock wave at the bottom of the impact plate. As indicated in the Introduction, the tilt of the wave front is grossly magnified over that of the projectile, and the sensitivity of the tilt-measuring system is thus heightened.

Three PZT gauges operating in open circuit mode are fixed to the bottom surface with outputs leading to transistors which amplify the first rise in the output and chop it to make a near-step function. This step is then fed to one of three switching circuits which turns a predetermined current into a power resistor. Steps from the three gauges are coded so that sequence of arrivals as well as their separations can be inferred from the stepped voltage across the power resistor. The resolution of the circuit is about 100 nsec, which corresponds to a tilt of about 0.01 radians.

3. Measurement of Stress Pulse Duration

As indicated earlier, the stress pulse duration is determined by the transit time of shock and rarefaction through the specimen. If the sample does not separate, it will eventually be re-shocked, perhaps many

times, and the stress history will be poorly known and probably too complicated for the analysis envisioned here. If the specimen is wrung onto the plate with a uniform thin layer of liquid, it is quite possible that the dynamic tensile strength of the liquid will exceed the magnitude of the tension produced on reflection. Consequently it may be necessary to screen liquids to find a suitable one, and it is therefore necessary to determine when the specimen separates from the plate relative to the time when the shock is incident on the free surface. An optical method is being examined for suitability:

The optically transparent sample is coupled to the bottom of the impact plate by a transparent liquid. A beam of light is focused through the LiF and liquid and onto the bottom surface of the impact plate. The beam is reflected off the impact plate and back through the specimen-liquid, then refocused onto a photomultiplier tube. As the specimen pulls free of the liquid the intensity of the reflected beam decreases, reducing the current output of the photomultiplier.

D. SAMPLE PREPARATION

LiF single crystals to be used in this study were purchased from the Harshaw Chemical Company. Two grades of purities were obtained with optical classifications of monochromatic (M) and vacuum ultra-violet (VUV). The latter is the highest purity available from Harshaw. The crystals were rod-like with square cross-sections and all faces were {100} planes. The quantities and sizes received were:

1) Monochromatic: ten - 0.5 cm x 0.5 cm x 2.6 cm long,

2) Vacuum Ultra-Violet: ten - 0.4 cm x 0.4 cm x 10 cm long.

Initially the VUV series was in a fully annealed state. Attempts to cleave the rods into platelets proved futile, for the process introduced fracture on the {110} planes before cleavage occurred on the {100} planes. The M-rods cleaved nicely, producing almost no cleavage steps. The VUV rods were sent back to Harshaw to be irradiated. Irradiation eliminated the cleaving problem.

Platelets with thicknesses near 1, 2, 3 and 4 mm have been cleaved from both materials. The VUV platelets were softened by annealing in a lava box for 50 hours at 600°C, and cooled at a rate of 20°C/hr. This seemed to eliminate all apparent effects of the irradiation treatment.

E. POLISHING AND ETCH-PIT ANALYSIS

Etch-pit techniques will be used for examination of dislocation behavior. This approach seems to provide a little more information than other methods.[2.2]

For both series of specimens, polishing and etching procedures have been established so that reliable examination can be made. The current polishing procedure consists of immersing a LiF specimen in a vigorously agitated solution of distilled water which contains one part per hundred of NH_4OH. The solution is kept at a temperature below 25°C. This results in a dissolution rate of ∿1 to 1.5 microns/second. It is observed, however, that prolonged polishing, i.e. greater than 30 minutes, sometimes produces a matte or "frosty" surface on the specimen. The reason for this behavior has not been determined, but should be resolved else dislocation density gradients through the interior of the specimen may not be reliably measured.

For etch-pit analysis two types of solutions are used:

1) Neutral solution: composed of distilled water with a very

small addition of $FeCl_3$ (Fe^{+3} ion helps inhibit the dissolution process.) It is believed[2.2] to form strong complexes with the F^- ion.

2) Acid etchant: consists of equal mixtures of concentrated HF and acetic acids with or without small additions of $FeCl_3$.

The etching characteristic of the two solutions are different. The neutral etchant distinguishes between "mobile" and "grown-in" dislocations. Sharp pyramidal pits are produced at the mobile dislocations, whereas only shallow and rather indistinct pits are observed at the grown-in (immobile) dislocations. The ability of the neutral etch to discriminate between mobile and grown-in dislocations is apparently due to a reduced sensitivity of attack brought about by the presence of impurities on the grown-in dislocations. This feature of the neutral etch is quite significant since the number of mobile and immobile dislocations can be determined. The acid etch, however, reveals both types of dislocations with equal distinction.

Etch-pit examination of the pre-stressed materials, employing etching times from 1 to 5 minutes, disclosed the following:

1) M-series: The initial dislocation density is $\rho_o \sim 10^4/cm^2$, of which nearly all appear to be immobile.

2) VUV, irradiated condition: $\rho_o \sim 10^6/cm^2$.

3) VUV, annealed: $\rho_o \sim 10^4/cm^2$, and a large percentage of these appear to be mobile dislocations.

4) The number of subgrains for both series ranges from one to three per specimen.

F. STATIC MECHANICAL DEFORMATION BEHAVIOR

A few tests have been carried out to gain some feeling for the deformation behavior of the two series of materials under "static" conditions.

These included macro-yield stress (in compression) and micro-hardness measurements. The former was done by an Instron machine using load rates of 0.05 cm/minute, whereas the latter was done on a Tukon hardness tester using a diamond pyramid indenter.

The static yield stress observed for the various materials were:

1) M-series: $\sigma_y \simeq 2$ kg/mm^2 ($\sim$3000 psi).
2) VUV-series in the irradiated condition: $\sigma_y \simeq 0.9$ kg/mm^2 ($\sim$1300 psi).
3) VUV-series in the annealed condition: $\sigma_y \simeq 0.17$ kg/mm^2 ($\sim$240 psi).

The microhardness measurements displayed the same trend as the yield stress.

Etch-pit studies on all materials tested were informative, especially those used for hardness measurements. For the compression specimens, the glide band behavior as reported by others[2.2, 2.3] was observed. The hardness indentations displayed rosette arrangements of dislocations, but the extent of generation for the annealed VUV series was much greater than for the others, especially for the M-series. These observations seem to confirm the initial etch-pit examination in terms of the number of mobile dislocations present for multiplication. As a result the VUV material in the annealed condition is the logical candidate for dynamic study.

G. FUTURE EFFORT

The following represent steps to be taken towards completion of this study:

1) Construction and alignment of new guide tube projectile system.
2) Completion of the tilt circuit and incorporation for tilt control for both impact systems.

3) Determine the limits of the parameters (velocity, stress, tilt and stress duration) associated with the low velocity impacts.

4) Proceed with dynamic dislocation multiplication study.

REFERENCES

2.1 J. J. Gilman, MICROMECHANICS OF FLOW IN SOLIDS, McGraw-Hill (1969)

2.2 J. J. Gilman and W. G. Johnston, "Dislocations in Lithium Fluoride Crystals," SOLID STATE PHYSICS, Vol. 13, p. 147 (1962)

2.3 W. G. Johnston and J. J. Gilman, "Dislocation Velocities, Dislocation Densities and Plastic Flow in Lithium Fluoride Crystals," J. Appl. Phys. 30, 129 (1959)

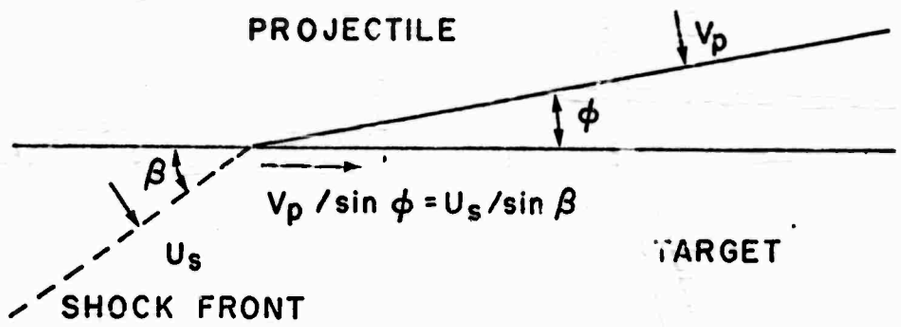

Figure 2.1 Effect of tilt on inclination of shock front

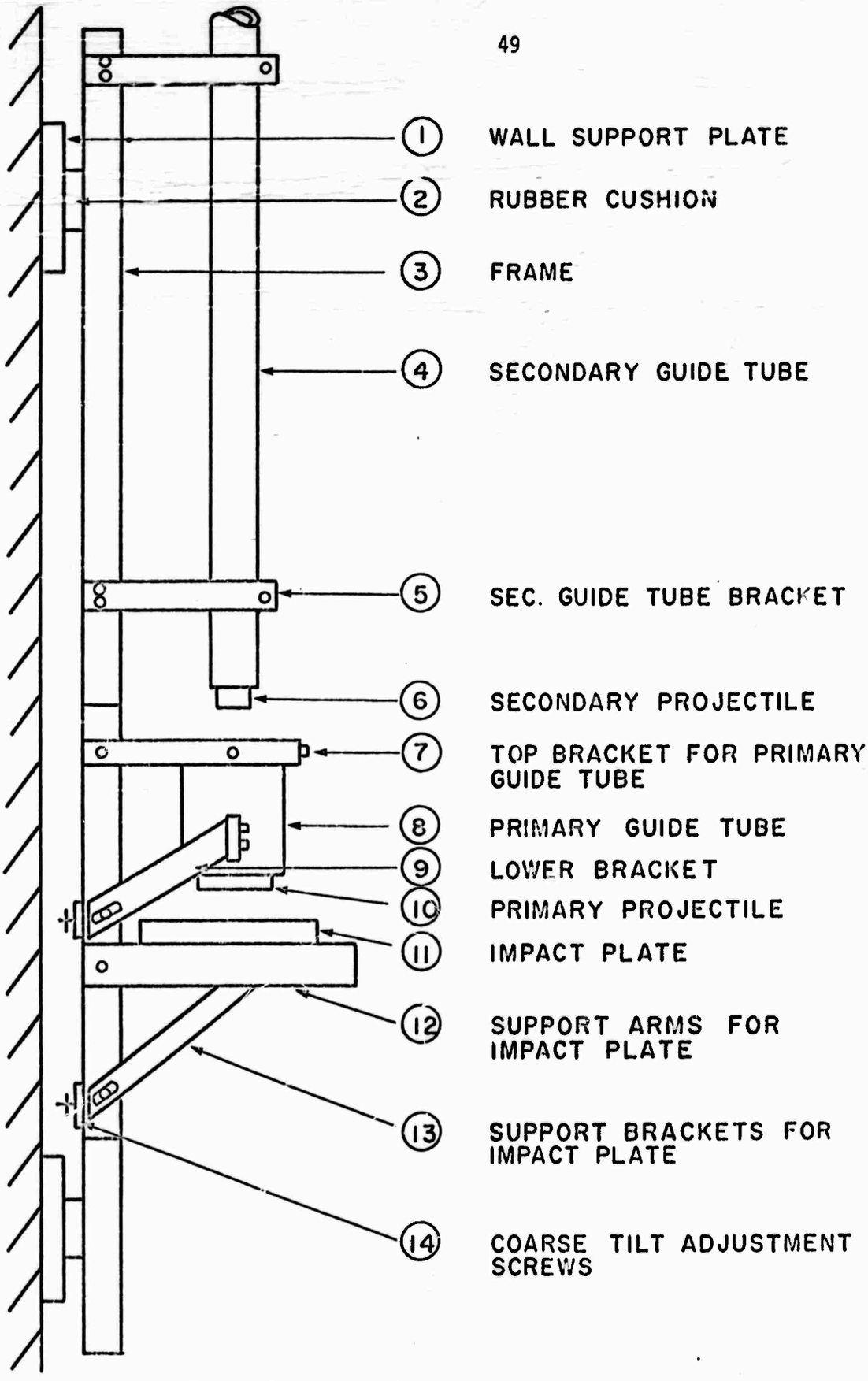

Figure 2.2 General schematic of the impact apparatus
Approximate scale, 3" = 16"

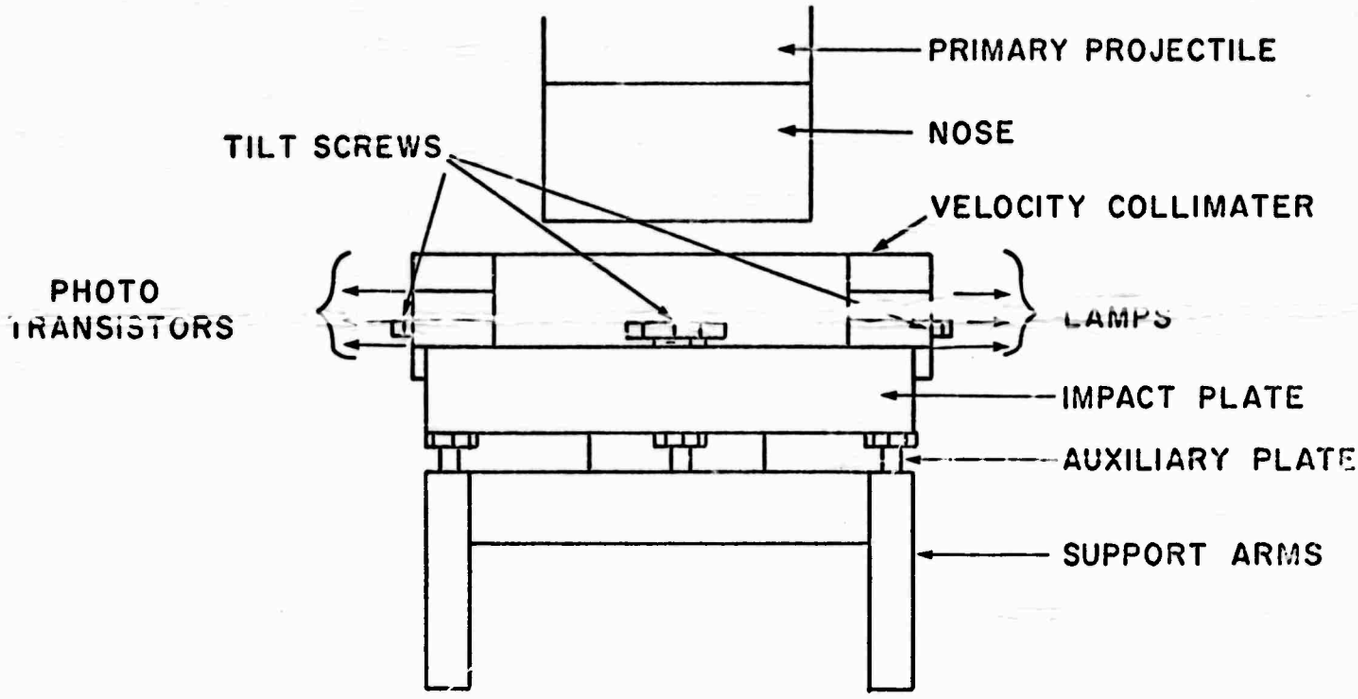

FRONT VIEW

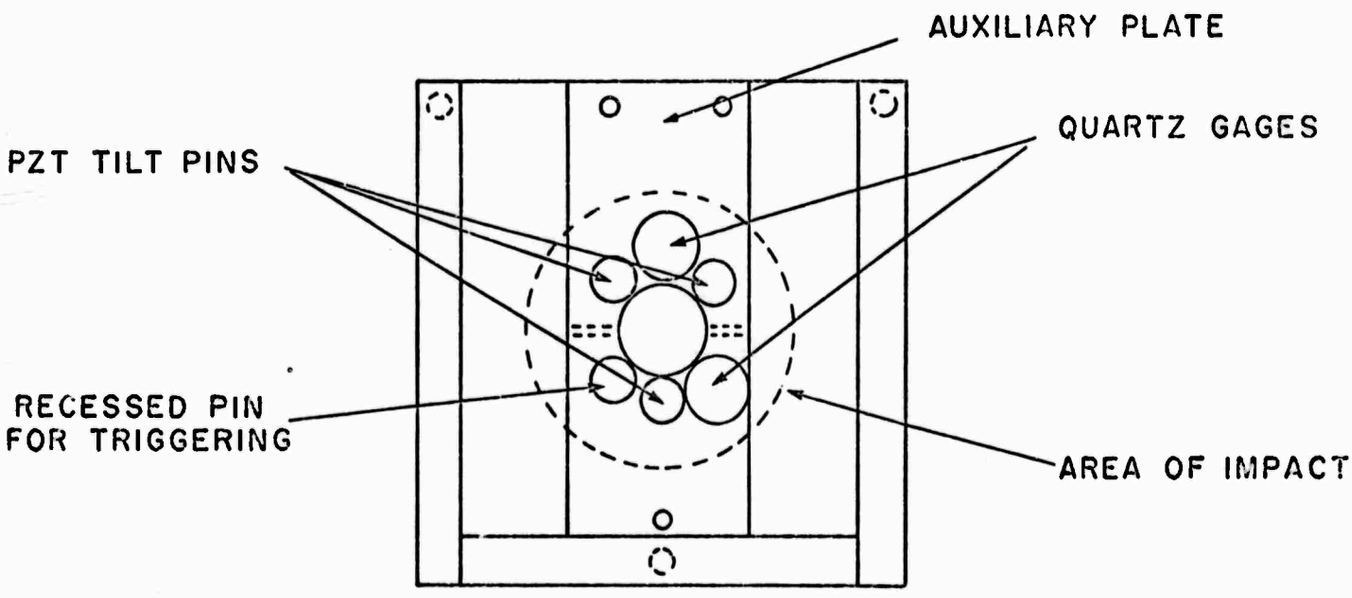

BOTTOM VIEW

Figure 2.3 Schematic layout of impact region

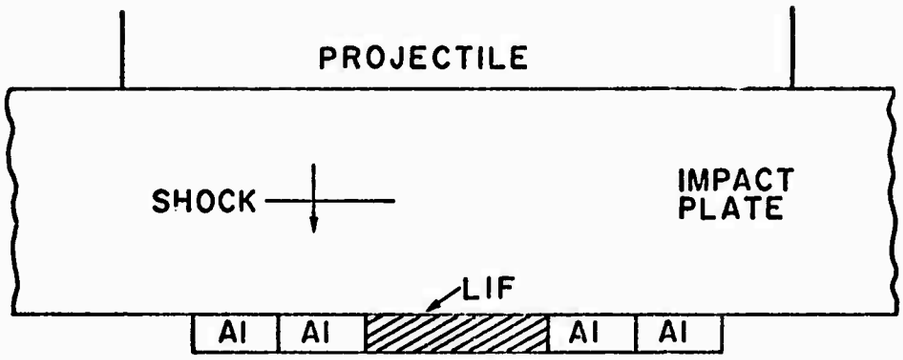

Figure 2.4 Arrangement of LiF specimen at bottom of impact plate

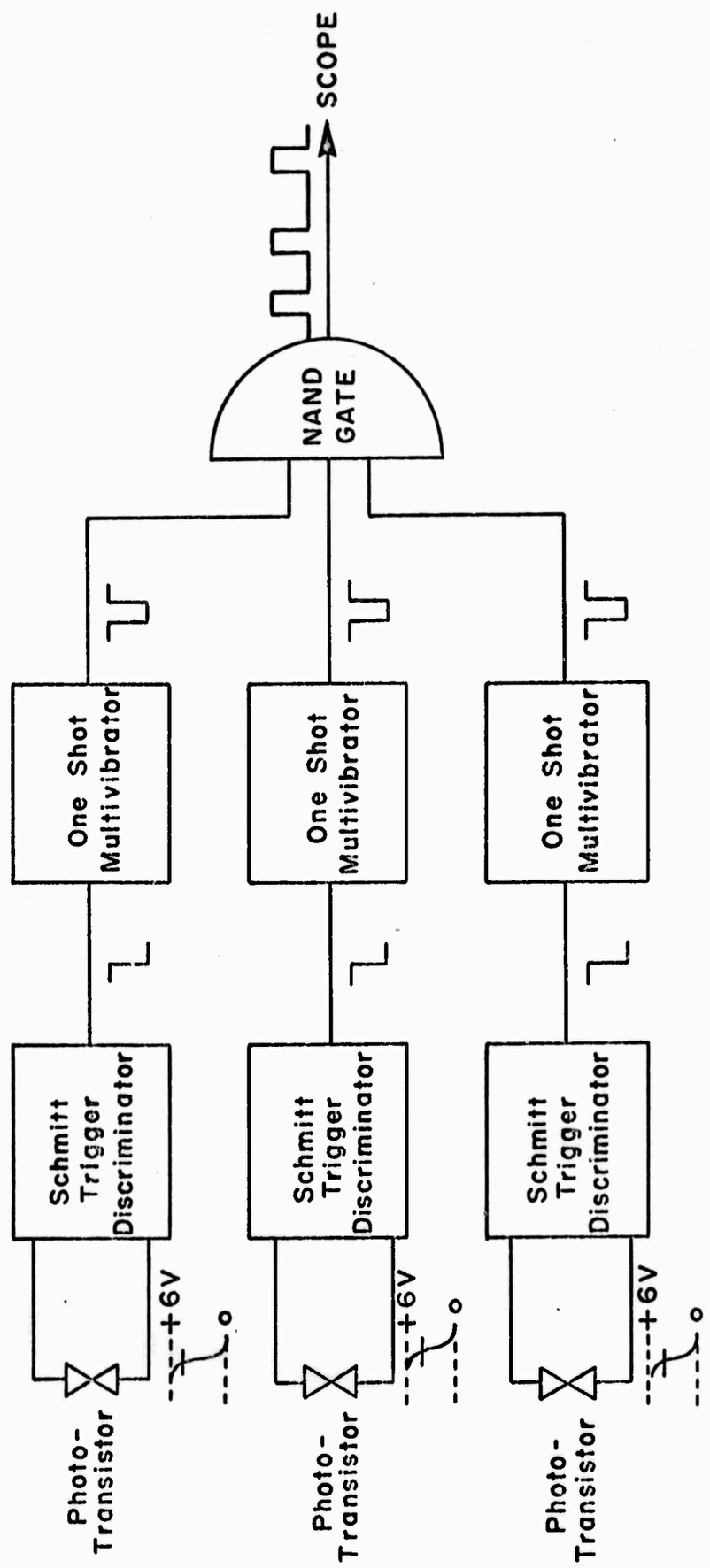

Figure 2.5 Photo-sensing Velocity System

III. WEAK SHOCK IMPEDANCE METHODS FOR THE QUARTZ GAUGE

J. W. Forbes, R. H. Mitchell

A. INTRODUCTION

A major effort in the shock wave field is now focused on the low stress region of materials. The experimental effort in the low stress region is due in part to the development of the quartz gauge.[3.1] It is the purpose of this paper to describe the impedance matching technique for reducing the measured pressure and particle speed in the quartz gauge to the pressure and particle speed in the sample material. This work will be restricted to materials which exhibit two shock waves resulting from a violation of the stability criterion.

The typical shock experiment (Fig. 3.1) is one where a projectile is incident on the front surface of a sample. The back surface is in contact with a quartz gauge. Upon impact two shock waves go forward (+ x direction) in the sample while a shock wave goes backwards (- x direction) in the projectile. The first shock in the sample reaches the quartz face and a shock wave is transmitted into the quartz. A rarefaction wave is reflected back into the sample if its impedance is higher than that of quartz. A shock wave is reflected if its impedance is less. Assume the backward facing wave and the forward facing second shock do not interact. The second shock then proceeds unperturbed to the quartz boundary, a shock wave is transmitted into the quartz, and a rarefaction or shock wave is reflected, depending on relative impedances of sample and quartz.

The state ahead of a weak shock or rarefaction wave is related to the state behind the wave by the Rankine-Hugoniot jump conditions.[3.2,3.3] Let

the subscript "o" represent the state ahead of the wave and the subscript "1" represent the state behind the wave.

$$\rho_o(D_1-u_o) = \rho_1(D_1-u_1) \tag{3.1}$$

$$P_1 - P_o = \rho_o(D_1-u_o)(u_1-u_o) \tag{3.2}$$

where ρ is density, D is wave speed, u is particle speed, and P is pressure.

Procedures for reducing quartz data to sample data are described here for three cases:

1) the sample is an elastic-plastic material with higher impedance than quartz,
2) it is a polymorphic material with higher impedance than quartz,
3) it is a material of lower impedance than quartz.

B. ELASTIC-PLASTIC MATERIAL OF HIGHER IMPEDANCE THAN QUARTZ

A simple solution to the impedance matching problem exists for this case. Assume that the rarefaction wave from the quartz boundary has the same speed as the elastic first shock wave in the material. The P-u plane describing the experiment is given in Fig. 3.2. A convenient but not necessary assumption is that the projectile material has a linear P-u relationship.

The first forward-facing elastic wave, D_1, shocks the material to state (P_1,u_1). The second forward-facing plastic shock wave, D_2, compresses the material to state (P_2,u_2). The backward-facing elastic wave, D_3, relieves the material from state (P_1,u_1) to the state (P_3,u_3). The second relief path from state (P_2,u_2) can be left unspecified; an arbitrary path is shown in Fig. 3.2. The state (P_2,u_2) is also defined by the backward-facing shock wave in the projectile.

Applying the Rankine-Hugoniot equations to the various states shown on the P-u diagram with $P_o=0$, $u_o=0$ results in the following set of equations.

$$\rho_o D_1 = \rho_1 (D_1 - u_1) \tag{3.3}$$

$$P_1 = \rho_o D_1 u_1 \tag{3.4}$$

$$P_2 - P_1 = \rho_1 (D_2 - u_1)(u_2 - u_1) \tag{3.5}$$

$$P_3 - P_1 = \rho_1 (D_1 + u_1)(u_1 - u_3) \tag{3.6}$$

$$P_2 = A + Bu_2 \tag{3.7}$$

The subscript indicates the material state behind the wave of the same subscript. The parameters known from the experiment are ρ_o, D_1, D_2, P_3, u_3, P_4, u_4, A and B. The constants A and B define the projectile's P-u relationship.

Solving these equations for the unknowns u_1 and P_1 results in

$$u_1 = \frac{D_1 (P_3 + \rho_o D_1 u_3)}{P_3 - \rho_o D_1 u_3 + 2\rho_o D_1^2} \tag{3.8}$$

$$P_1 = \frac{\rho_o D_1^2 (P_3 + \rho_o D_1 u_3)}{P_3 - \rho_o D_1 u_3 + 2\rho_o D_1^2} \tag{3.9}$$

Using the results of Eqs. (3.8) and (3.9), P_2 becomes

$$P_2 = \frac{P_1 B - \rho_1 (D_2 - u_1)(A + Bu_1)}{B - \rho_1 (D_2 - u_1)} \tag{3.10}$$

The relief path for the second wave has not been used in the above results.

A test of relief modes for the second wave can in principle be made by assuming a model and comparing the results for P_2 with Eq. (3.10).

C. POLYMORPHIC MATERIAL WITH IMPEDANCE HIGHER THAN QUARTZ

The solution to this problem requires an assumption about the equation of state. The assumption made here is that the first phase of the material has a linear shock speed-particle speed, (U_s-U_p), relation. It is also assumed that the bulk sound speed, c_o, at STP conditions is known.

The P-u plane is shown in Fig. 3.3. The state of the material behind the first shock, D_1, is (P_1,u_1). The state behind the second shock, D_2, is (P_2,u_2). The backward-facing rarefaction wave from the quartz face takes the material from state (P_1,u_1) to state (P_3,u_3). The second rarefaction fan takes the material from state (P_2,u_2) to state (P_4,u_4). The state (P_2,u_2) is also defined by the backward shock wave in the projectile.

The state $(P_3,2u_1-u_3)$ is symmetric to (P_3,u_3) and contains the same information as (P_3,u_3). A hypothetical forward facing shock D_3^+ would take the material from state $(P_3,2u_1-u_3)$ to state (P_1,u_1).

The Rankine-Hugoniot equations can be applied to the various states on the P-u curve with $P_o=0$, $u_o=0$, resulting in the following set of equations:

$$\rho_o D_1 = \rho_1(D_1-u_1) \tag{3.3B}$$

$$P_1 = \rho_o D_1 u_1 \tag{3.4B}$$

$$P_2-P_1 = \rho_1(D_2-u_1)(u_2-u_1) \tag{3.5B}$$

$$P_2 = A + Bu_2 \tag{3.7B}$$

$$P_3-P_1 = \rho_1(D_3^+-u_1)(u_1-u_3) \tag{3.11B}$$

$$D_1 = c_o + Su_1 \tag{3.16}$$

$$D_3^+ = D_1 - S(u_3 - u_1) \tag{3.17}$$

The subscript indicates the material state behind the wave of the same subscript. The parameters known from the experiment are ρ_o, D_1, D_2, P_3, u_3, P_4, u_4, A and B; the constants A and B define the projectile's P-u relationship.

The state symmetric to (P_3,u_3) lies on the first phase of the P-u branch. The symmetric state $(P_3,2u_1-u_3)$ has been used for Eqs. (3.11B) and (3.17). Eqs. (3.16) and (3.17) represent the linear U_s-U_p relation assumed for the first phase.

The analytical solution is difficult, but numerical solutions are readily found. A flow chart for numerical solution is given in Fig. 3.4. The procedure is started by choosing a value for u_1 and calculating all the unknown parameters related to the first shock wave in the material. The calculated pressure P_3 is compared to the measured P_3. The value of u_1 is increased by Δ if the two numbers disagree and the process is repeated until they agree; the solution for the first phase is then complete. The elimination of P_2 between Eqs. (3.5B) and (3.7B) allows calculation of u_2; calculation of P_2 from Eq. (3.7B) completes the solution.

The relief path for the second wave has not been used in the above results. A test of relief models for the second wave can in principle be made.

D. MATERIALS WITH IMPEDANCE LOWER THAN QUARTZ

The solution to this problem requires an assumption about the equation of state. The assumption made here is that the second phase of the material has a linear U_s-U_p relation.

The P-u plane for a material of lower impedance than quartz is given in Fig. 3.5. The state of the material behind the first shock, D_1, is defined by (P_1,u_1). The state behind the second shock, D_2, is defined by (P_2,u_2). The first backward-facing shock, D_3, takes the material from state (P_1,u_1) to (P_3,u_3). The second backward-facing shock from the quartz face takes the sample from state (P_2,u_2) to state (P_4,u_4). The state (P_2,u_2) is also defined by the backward shock wave in the projectile.

The state $(P_3,2u_1-u_3)$ is symmetric to (P_3,u_3) and contains the same information as (P_3,u_3). The state $(P_4,2u_2-u_4)$ is symmetric to (P_4,u_4) and contains the same information as (P_4,u_4).

The Rankine-Hugoniot equations can be applied to the various states on the P-u plane with $P_o=0$, $u_o=0$, resulting in the following set of equations.

$$\rho_o D_1 = \rho_1(D_1-u_1) \tag{3.3A}$$

$$P_1 = \rho_o D_1 u_1 \tag{3.4A}$$

$$P_2-P_1 = \rho_1(D_2-u_1)(u_2-u_1) \tag{3.5A}$$

$$P_2 = A + Bu_2 \tag{3.7A}$$

$$P_3-P_1 = \rho_1(D_3^+-u_1)(u_1-u_3) \tag{3.11}$$

$$P_4-P_2 = \rho_2(D_4^+-u_2)(u_2-u_4) \tag{3.12}$$

$$\rho_1(D_2-u_1) = \rho_2(D_2-u_2) \tag{3.13}$$

$$D_2 = D_3^+ + S(u_2+u_3-2u_1) \tag{3.14}$$

$$D_4^+ = D_2 + S(u_2-u_4) \tag{3.15}$$

The subscript indicates the state behind the wave of the same subscript. The states symmetric to (P_3,u_3) and (P_4,u_4) lie on the P-u branch for the second phase. The symmetric states have been used for Eqs. (3.11), (3.12), (3.13), and (3.14). A hypothetical forward-facing shock, D_3^+, would change the material from state $(P_3,2u_1-u_3)$ to (P_2,u_2). A hypothetical forward-facing shock, D_4^+, would change the material from state (P_2,u_2) to $(P_4,2u_2-u_4)$.

Equations (3.14) and (3.15) represent the assumed U_s-U_p relation. Known parameters from the experiment are ρ_o, D_1, D_2, P_3, u_3, P_4, u_4, A and B. Parameters A and B define the linear P-u relationship for the projectile.

Analytical solution of the nine equations is difficult and possibly unattainable, but they can be solved numerically. A flow chart for the numerical solution is shown in Fig. 3.6.

The procedure described in Fig. 3.6 is started by choosing a value for u_1 and calculating all the other unknowns. The calculated pressure P_3 is compared to the measured value of P_3. If they disagree, u_1 is increased by Δ and the process repeated until they do agree. Choosing u_1 as the parameter to change makes it possible to use most of the equations of the set in their given form. The one exception to this is that Eqs. (3.5A) and (3.7A) need to be solved for u_2 by eliminating P_2 from the equation.

The above procedure is illustrated for Cadmium sulfide-lucite composites, which have lower impedance than quartz. CdS undergoes a polymorphic phase transition at about 30 kilobars, and two waves are formed if the driving pressure is in the right range. The data from two experiments with results of calculations for P_1 and P_2 are given in Table IX. The projectile material was 6061-T6 aluminum.

REFERENCES

3.1 R. A. Graham, F. W. Neilson, and W. B. Benedick, J. Appl. Phys. 36, 1775 (1965)

3.2 M. H. Rice, R. G. McQueen, and J. M. Walsh, SOLID STATE PHYSICS, Vol. 6, 1-63 (1958)

3.3 G. E. Duvall and G. R. Fowles, HIGH PRESSURE PHYSICS AND CHEMISTRY, Vol. 2, 209-291 (1963)

TABLE IX

DOUBLE SHOCK WAVE IN CdS

Shot Number	69-005	69-036
Sample Density (gm/cm^3)	1.785	2.025
D_1 (cm/μsec)	.2860	.2955
D_2 (cm/μsec)	.2780	.2938
P_3 (megabars)	.0365	.0332
u_3 (cm/μsec)	.0237	.0217
P_4 (megabars)	.0496	.0440
u_4 (cm/μsec)	.0322	.0285
Projectile Speed (cm/μsec)	.0869	.0777
A (megabars)	.1244	.1113
B (megabar cm/μsec)	-1.42	-1.42
Transition Pressure P_1 (megabars)	.0244	.0230
Final Pressure, P_2 (megabars)	.0327	.0330

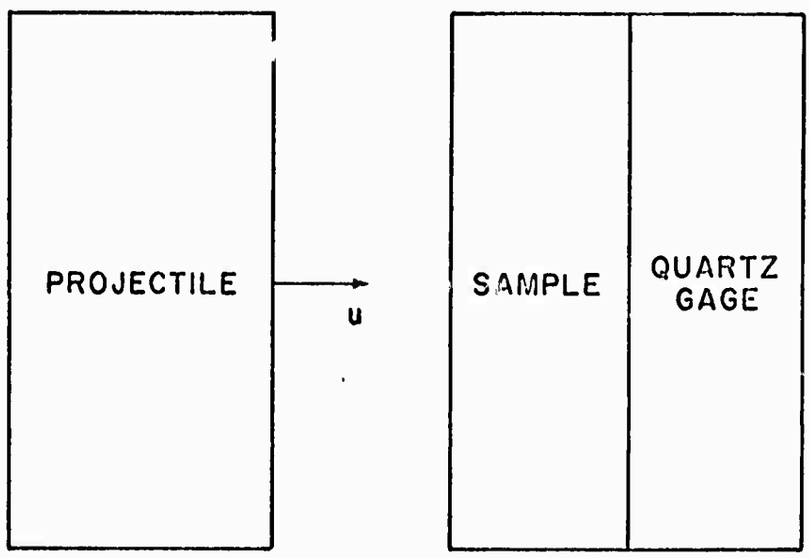

Figure 3.1 Typical shockwave experiment

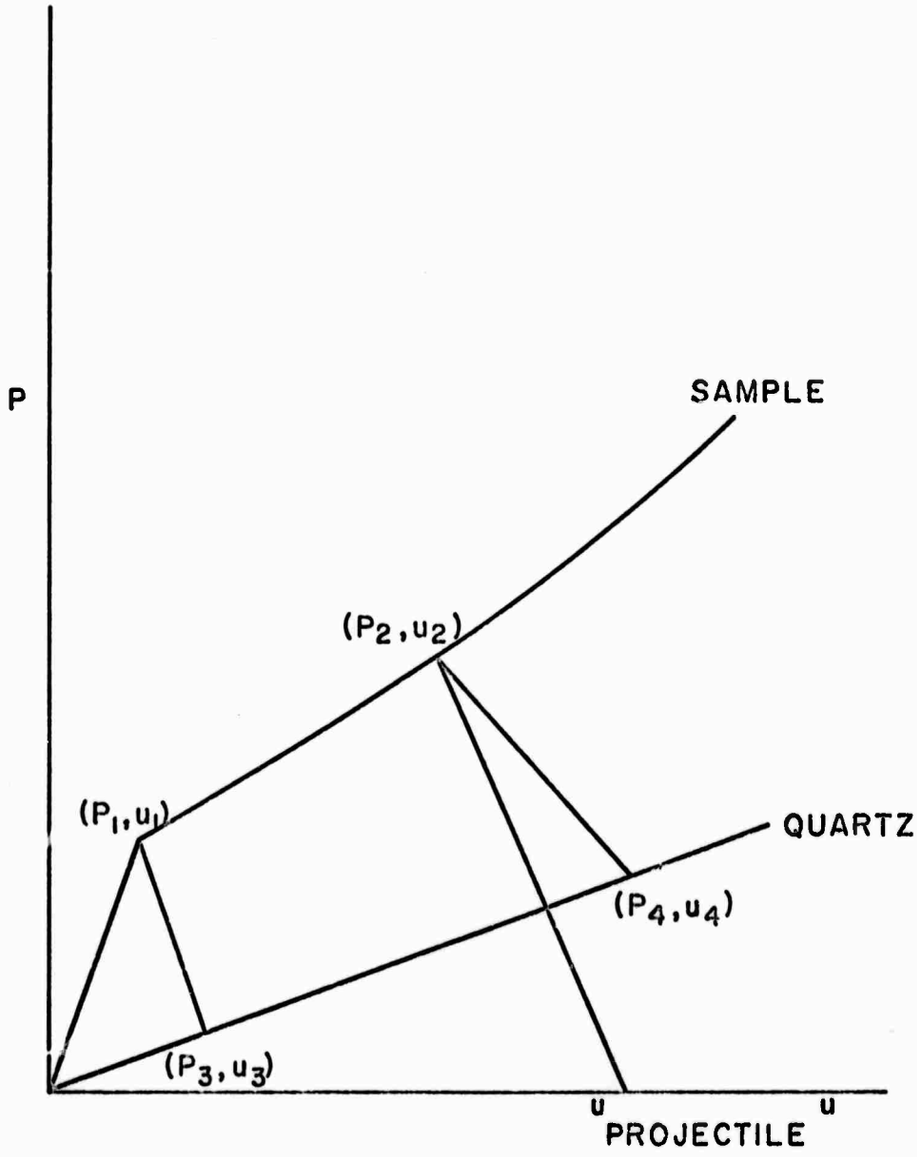

Figure 3.2 P-u plane of elastic-plastic material of higher impedance than quartz.

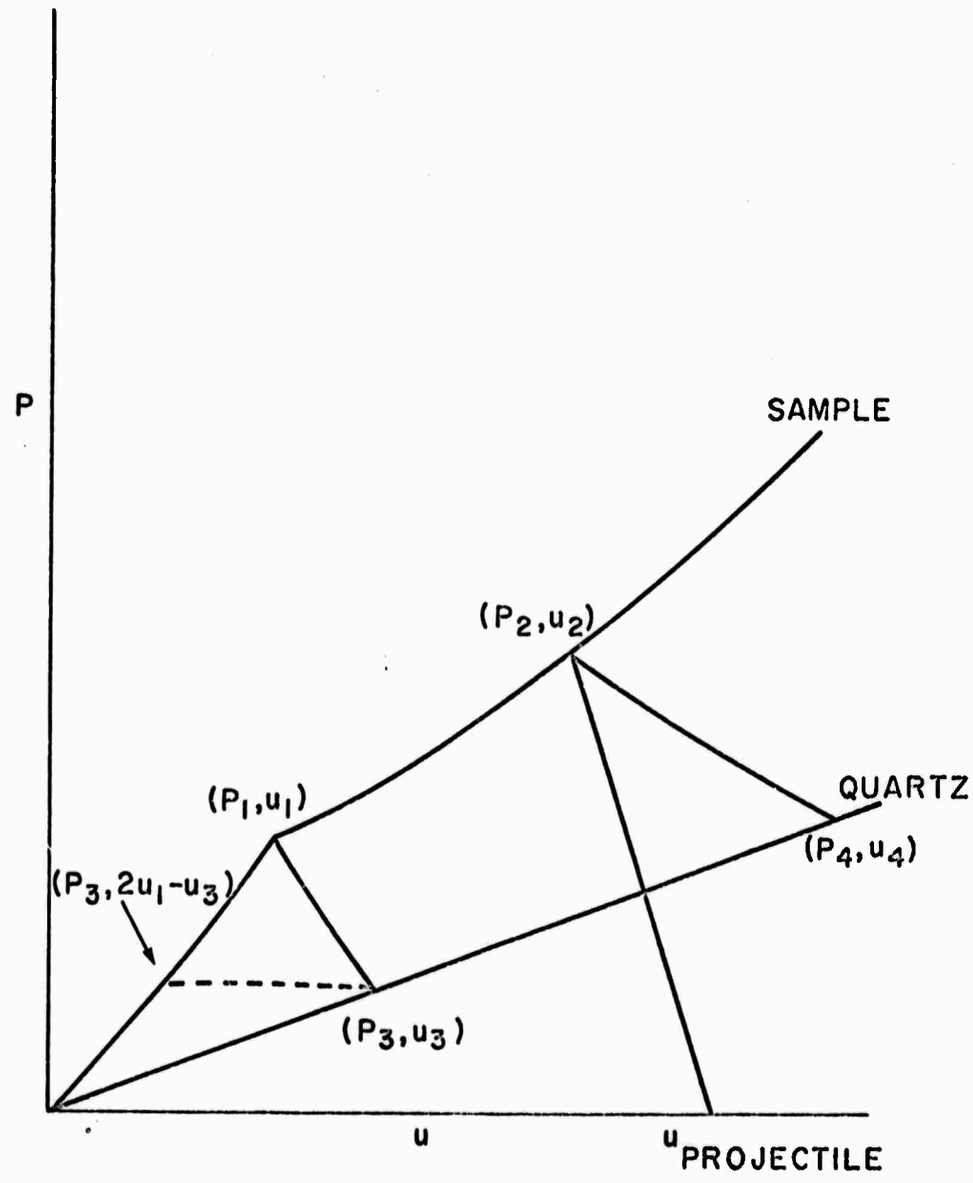

Figure 3.3 P-u plane of polymorphic material with a higher impedance than quartz.

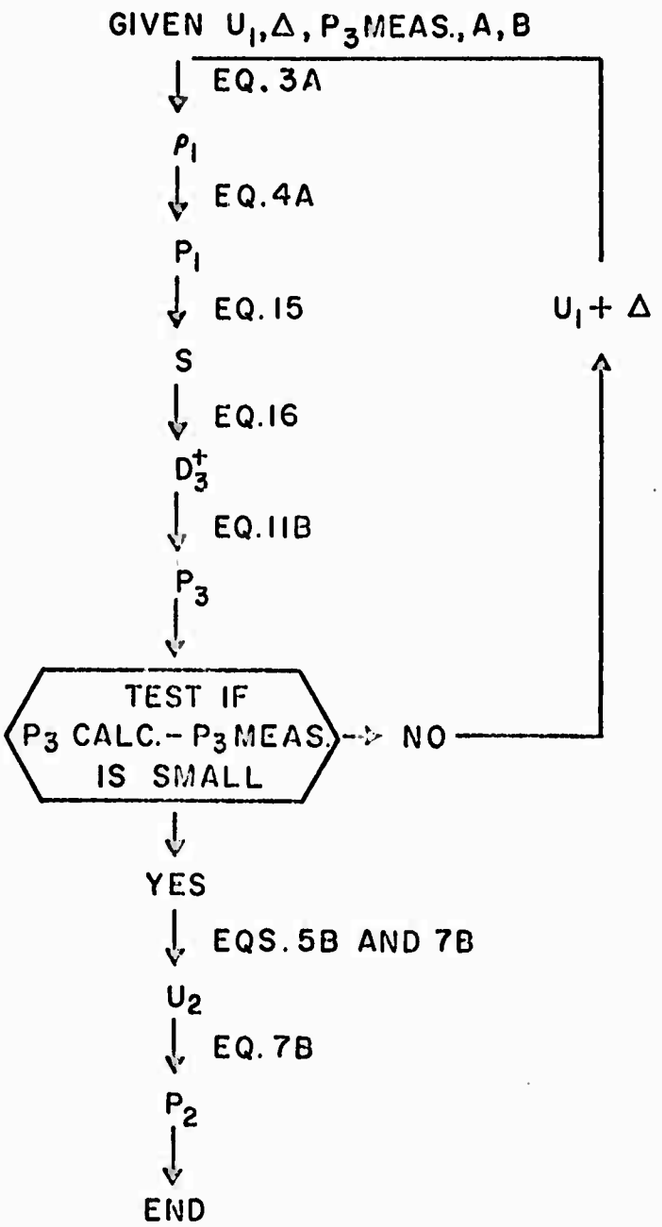

Figure 3.4 Flow of numerical impedance calculation for polymorphic material of higher impedance than quartz.

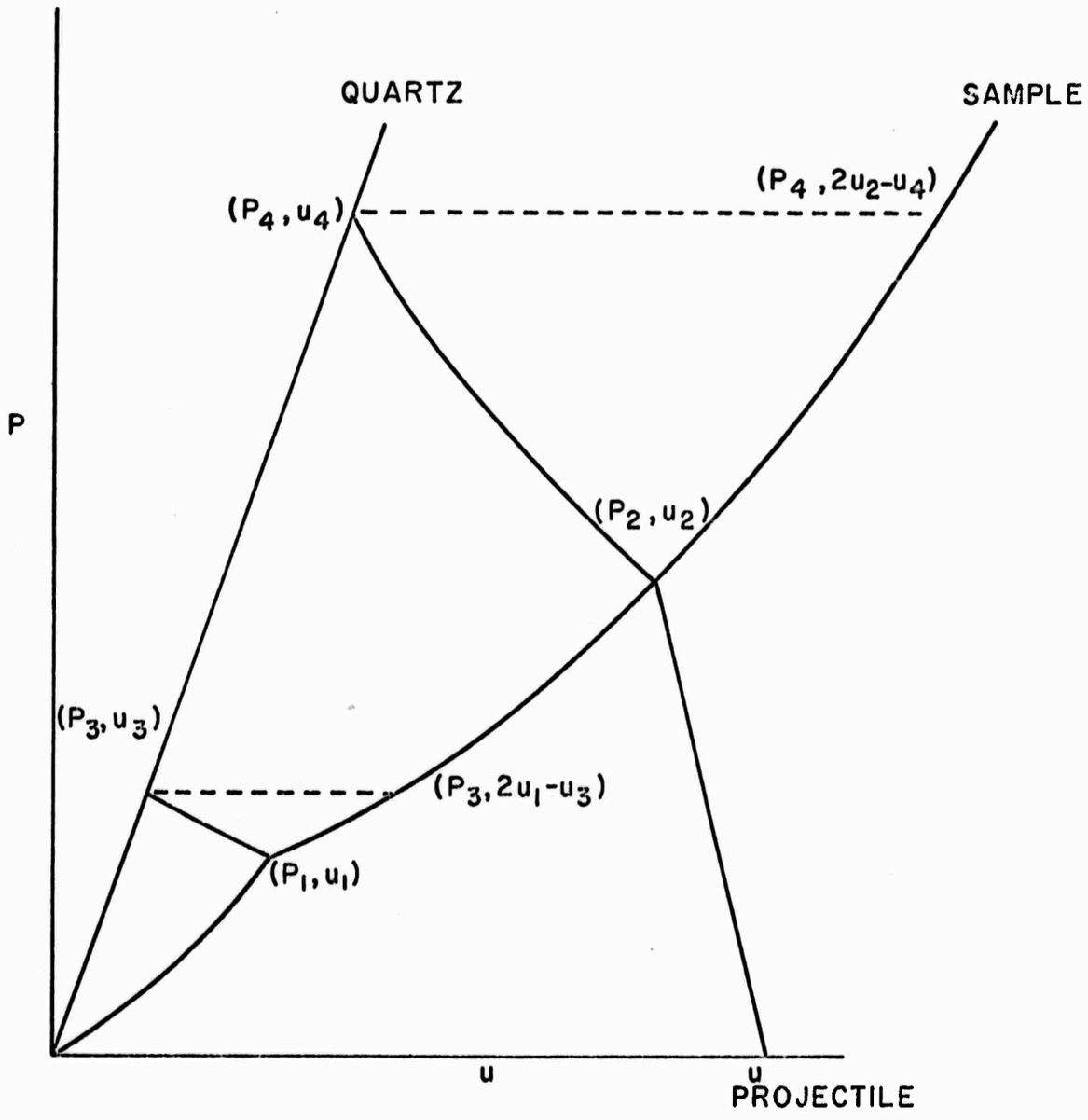

Figure 3.5 P-u plane of material with a lower impedance than quartz.

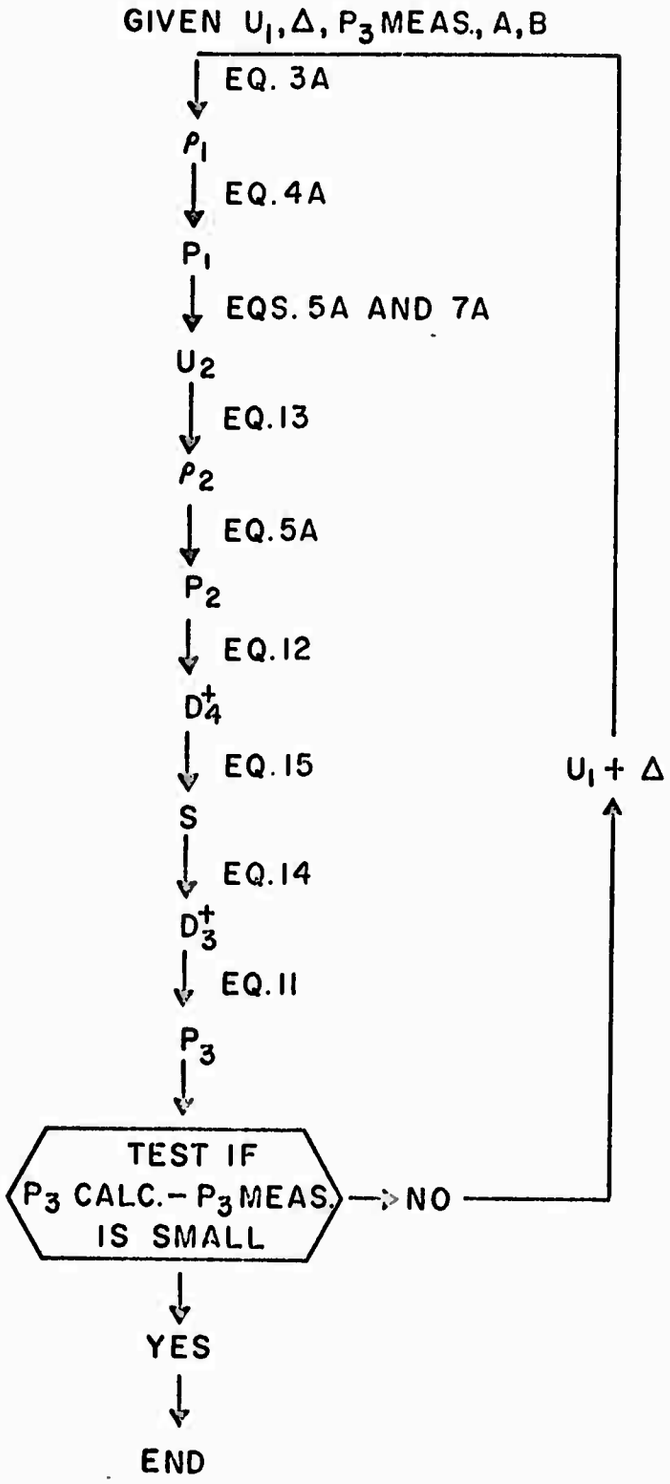

Figure 3.6 Flow of numerical impedance calculation for materials of lower impedance than quartz.

IV. SHOCK COMPRESSION OF CdS

R. H. Mitchell

A. INTRODUCTION

CdS is known to undergo a phase transformation at a static pressure of 27 kbar. This transformation from a wurtzite to a rocksalt structure is accompanied by a 19% change in specific volume.[4.1] Kennedy and Benedick report this transition under shock loading conditions at 31.5 kb and 28 kb respectively in single crystals shock-loaded parallel to the C-crystal axis and perpendicular to it.[4.2] They base their findings on an observed double wave structure and on the calculated change in specific volume. However, the elastic waves in CdS single crystals (42 kb for the C-axis and 21 kb perpendicular to it) will themselves give rise to double wave structures. There is thus some uncertainty whether the observed two-wave structure is due to the phase change. The object of the work reported here was twofold; first, to determine if a phase change does in fact occur under shock loading conditions, and second, to establish the transition pressure in an experimental situation which minimizes the effects of the elastic precursor.

B. METHOD OF MIXTURES

If the elastic limit can be reduced to zero, shock experiments will yield essentially hydrostatic pressure-volume data. To accomplish this a method similar to that employed by Dremin and Karpukhin was used.[4.3] This method consists of mixing the material under study with another material of known characteristics. Lucite, which has a well-known Hugoniot and a very low elastic limit, was selected as the second component of the matrix.

The lucite used had a density of 1.18 gr/cc. CdS has a density of 4.82 gr/cc.

To prepare the samples of this matrix the two components are first thoroughly mixed in a ball mill for a period of twenty-four hours. The mixture is then placed in a mold under a pressure of 4000 psi and at a temperature of 160°C. It is allowed to remain in this state for a period of one-half hour, during which time the lucite melts and flows evenly around all of the CdS particles. In all the samples molded no porosity was observed.

From an examination of the wave profile obtained during an impact experiment on one of these samples it is possible to determine if a phase transition in the CdS occurs. For the wave profile to be indicative of the actual state of the material, the particle size of the CdS must be considered. If the particles are too large the shock wave will be smeared out, giving the same effect as if the tilt were increased. This is due to the fact that the wave has a different velocity in the two matrix components. In this series of shots all apparent tilts were consistent with the measured mechanical tilt of the projectile.

The minimum particle size allowable is determined by the following. Since CdS and lucite have different mechanical properties, particles of these materials will reach different temperatures during a given shock compression. To be able to use Hugoniot data for the lucite the size of the particles must be such that this temperature difference doesn't have time to equilibrate during the shock compression. If the time of the process is given as τ and the thermal diffusivity as χ, then an estimate of the minimum size of the particles is $\ell \sim \sqrt{\chi\tau}$. This gives us 0.5 - 1.0 μ for times on

the order of a microsecond. The CdS particles ranged from 44 to 250 μ with 150 μ being the average size. The characteristic dimension of the lucite ranged from 20 to 100 μ with 60 μ being the average size. These values are well above the minimum particle size.

C. TARGET PREPARATION

To prepare specimens for use, thick samples are first molded as described in Section B. These are then surface ground on both sides to reduce them to the desired thickness. After surface grinding, the specimens are lapped until their surfaces are parallel to within 1×10^{-4} radians. A quartz gauge is then epoxied onto the rear surface of the specimen. This bonding layer of epoxy between the specimen and gauge is measured and has been found in every case to be less than 1×10^{-4} inches. This specimen-quartz sandwich is then epoxied into the brass target cup which provides electrical shielding for the quartz gauge. This cup is closed on the back with a brass cap that has a small hole in it to bring out the signal cable. Located symmetrically around this cup are four hollow conducting tilt pins. The final assembly is then lapped to insure that the tilt pins and specimen surface lie in a single plane. Also in the target is a ground pin which is turned out a few thousandths of an inch to ground the projectile just before impact. One final check is made on the specimen thickness after the final lap is accomplished. Finally the target cup is poured nearly full of epoxy covering the signal developing resistor and sealing the leads. A typical target assembly is shown in section in Figure 4.1.

D. EXPERIMENTAL RESULTS

Five shots with six specimens were fired. The wave profiles in the CdS-lucite matrix obtained by impedance matching are shown in Fig. 4.2.

These profiles were reduced from the quartz profiles by the procedure described in Section III.

The results are not definitive, but they indicate the following: 027 and 017 show no indication of a transformation. 015 and 036 show a transformation occurring at 23 kb. 005 shows the transformation at 24.5 kb. Apparently the transformation pressure is a function of the driving stress, requiring something greater than 30 kb to initiate. With increased driving stress the transition pressure increases as shown by 005. In this shot the transformation pressure has increased 1.5 kb for an increase in driving stress of 4.5 kb.

Figures 4.3 and 4.4 are pressure-volume plots of the three shots exhibiting the transformation. Any particular shot yields three data points on the P-V diagram, the first being the initial volume of the specimen, the second being the volume at the transition, and the third being the volume of the final state. The horizontal line in both diagrams is the calculated 19% volume change diminished to ~5% by the dilution with lucite. Note that the upper branch of the curve is steeper than the lower branch, as you would expect. The data and computations are summarized in Tables X and XI.

REFERENCES

4.1 S. S. Kabalkina and Z. V. Troitskaya, Soviet Physics/Doklady 8, 700 (1964)

4.2 J. D. Kennedy and W. B. Benedick, J. Phys. Chem. Solids 27, 125 (1966)

4.3 A. N. Dremin and I. A. Karpukhin, Zhurnal Prikladnoi Mekhaniki i Tekhnicheskoi Fiziki 3, 184 (1960)

PRELIMINARY DATA

TABLE X

DATA AND COMPUTATIONS

Shot Number	Sample Number	P_1 Transition Pressure (Kb)	P_2 Peak Pressure (Kb)	Sample Density (gr/cc)	Initial Specific Volume (cc/gr)	Specific Volume at Transition (cc/gr)	Specific Volume at Peak Pressure (cc/gr)
69-005	1	24.5	37.5	1.785	.5602	.4669	.405
69-015	1	23	33	2.016	.496	.4371	.4059
69-017	1	----	30	2.025	.4938	-----	.4207
69-027	1	----	27	2.025	.4938	-----	.391
69-027	6	----	26.5	2.121	.4715	-----	.3735
69-036	3	23	33	2.025	.4938	.4296	.4013

PRELIMINARY DATA

TABLE XI

DATA AND COMPUTATIONS

Shot Number	Sample Number	Sample[a] Thickness (mm)	P_3 (Kb)	U_3 (mm/μsec)	P_5 (Kb)	U_5 (mm/μsec)	D_1 (mm/μsec)	D_2 (mm/μsec)	% CdS by Weight
69-005	1	5.67	36.5	.237	49.6	.322	2.86	2.78	44.88
69-015	1	6.16	b	b	b	b	3.10	3.06	54.91
69-017	1	5.258	38.2	.245	----	----	3.00	----	55.26
69-027	1	3.96	40	.260	----	----	2.50	----	55.26
69-027	6	5.73	37	.240	----	----	2.48	----	58.75
69-036	3	5.375	33.2	.215	44	.285	2.955	2.938	55.26

[a]All samples were 31.75 mm in diameter

[b]These columns not applicable as shot 69-015 used a manganin gauge.

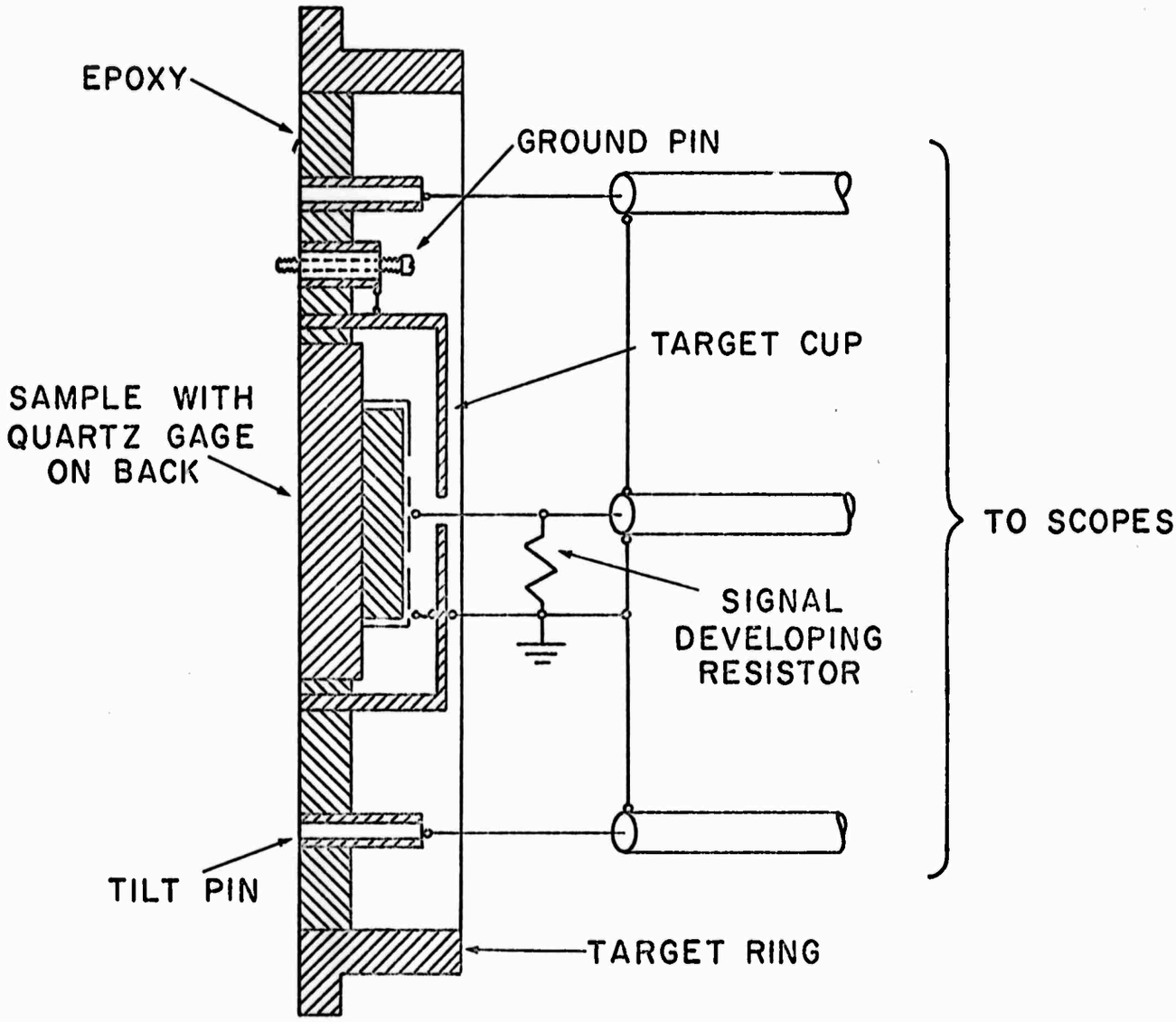

TYPICAL TARGET ASSEMBLY

Figure 4.1

PRELIMINARY DATA

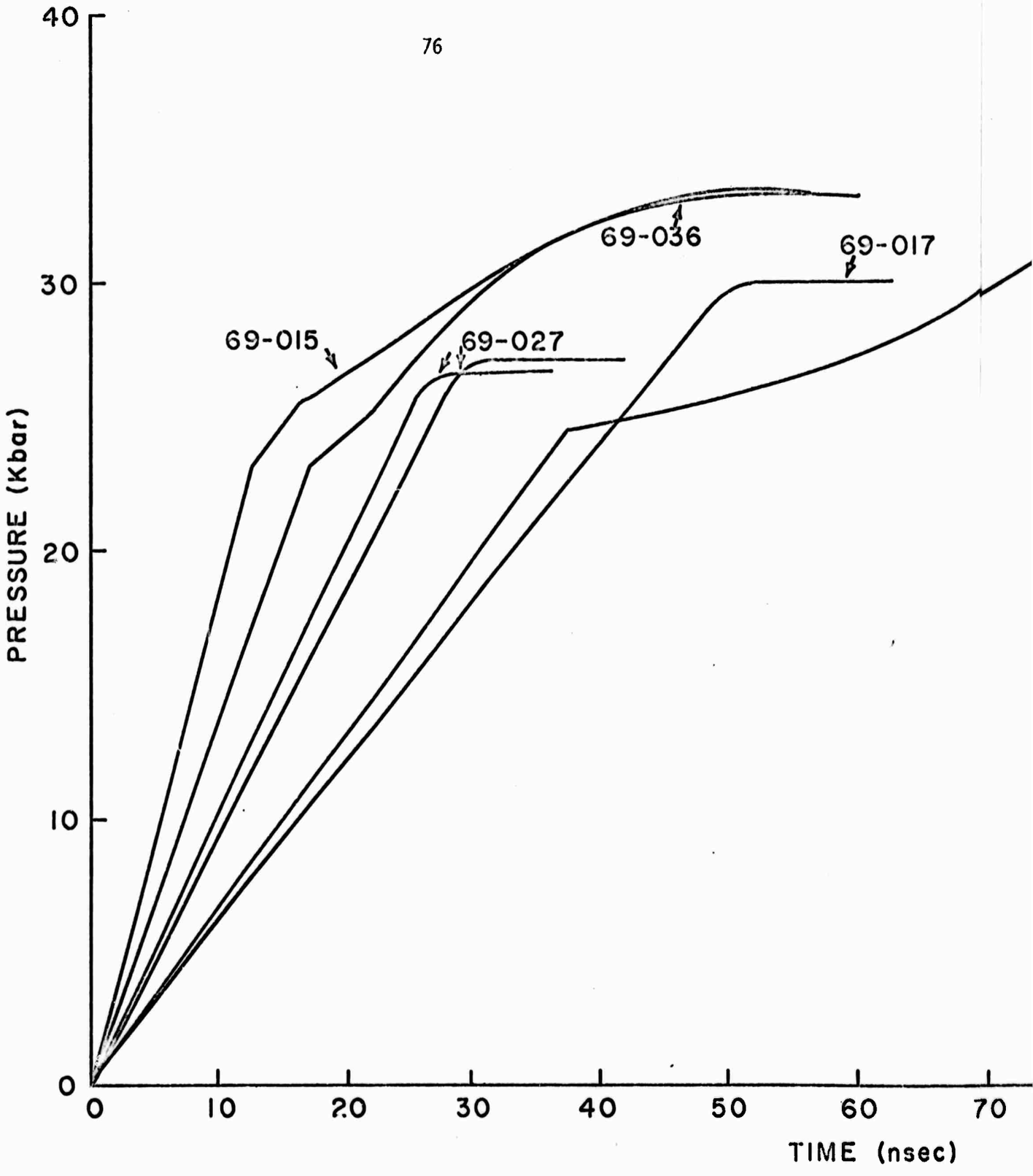

WAVE PROFILES IN CdS

Figure 4.2

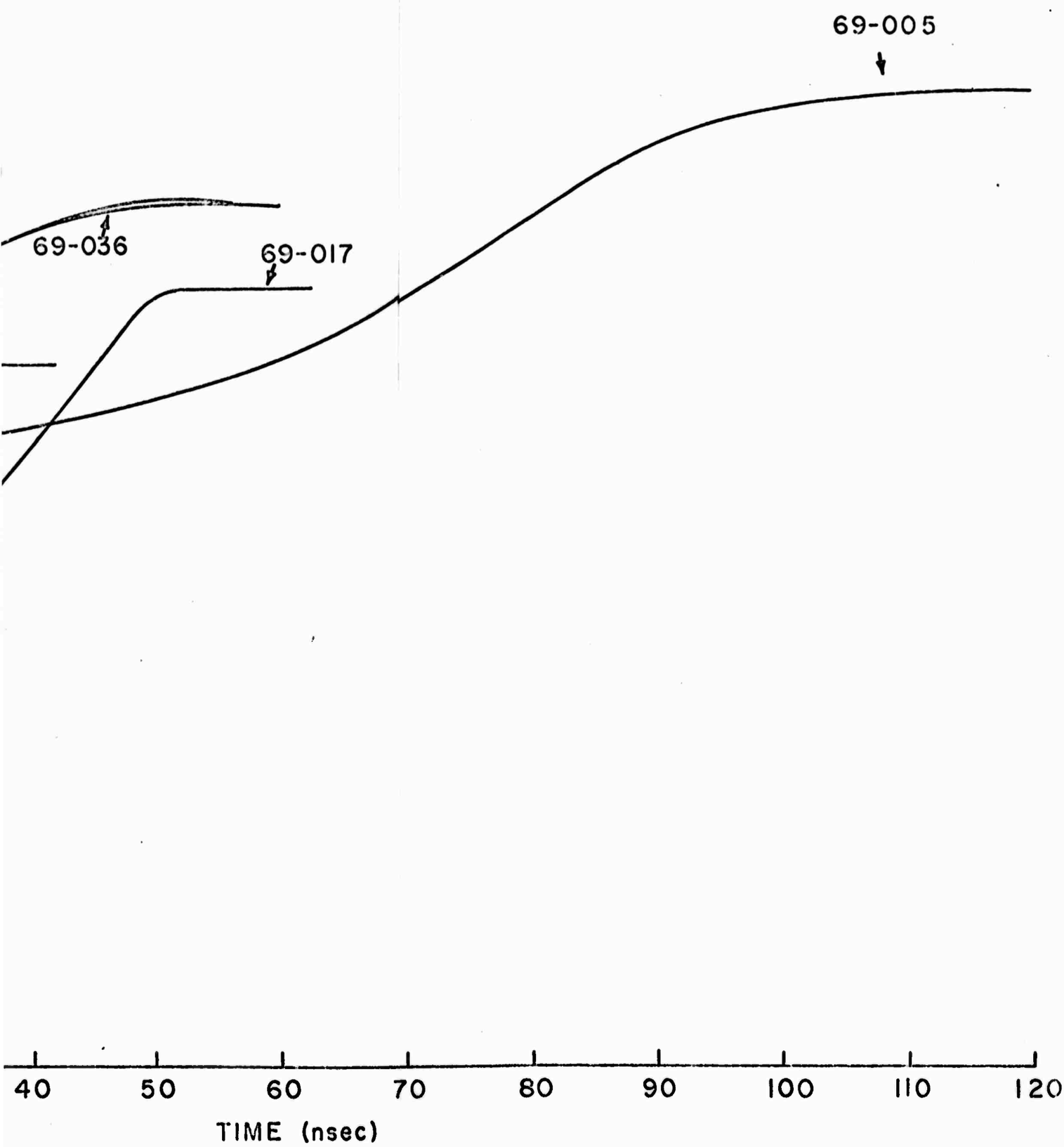

'AVE PROFILES IN CdS MATRIX

Figure 4.2


SHOT 69-015 & 69-036
PRESSURE (Kbar)
35
30
25
20
15
10
5
0
.40
.42
.44
.46
.48
.50
SPECIFIC VOLUME (cc/gm)
Δ SHOT 69-015
O SHOT 69-036

Figure 4.3


SHOT 69-005
PRESSURE (Kbar)
40
35
30
25
20
15
10
5
0
.40
.42
.44
.46
.48
.50
.52
.54
.56
SPECIFIC VOLUME (cc/gm)

Figure 4.4

V. REPORTS, PUBLICATIONS & PAPERS

G. R. Fowles, "Determination of Constitutive Relations from Plane Wave Experiments," Paper presented at Western Applied Mechanics Conference, Albuquerque, N.M., 25 - 27 August 1969.

J. R. Asay, G. E. Duvall, & M. H. Miles, "Elastic Precursor Decay in LiF," Bull. Amer. Phys. Soc., Series II, Vol. 14, #12, p. 1170, (Dec. 1969)

T. E. Michaels & G. E. Duvall, "Elastic Precursor Decay in Single Crystal Tungsten," Bull. Amer. Phys. Soc., Series II, Vol. 14, #12, p. 1170, (Dec. 1969)

Dennis E. Grady, "A Constant Current Source for Manganin Gauge Transducers," Rev. of Scientific Instruments, 40, #11, 1399-1402, (Nov. 1969)

Richard Fowles & Roger F. Williams, "Plane Stress Wave Propagation in Solids," J. Appl. Phys., 41, #1, p. 360, (1970)

S. C. Lowell, "Wave Propagation in Monatomic Lattices with Anharmonic Potential," Proc. Royal Soc. London A, to be published summer 1970.

Richard Fowles, "Determination of Constitutive Relations from Plane Wave Experiments," WSU SDL 70-01 (April 1970)

J. N. Johnson, O. E. Jones and T. E. Michaels, "Dislocation Dynamics and Single-Crystal Constitutive Relations: Shock Wave Propagation and Precursor Decay," J. Appl. Phys., 41, #6, p. 2330, (May 1970)

G. R. Fowles, G. E. Duvall, J. R. Asay, P. Bellamy, F. Feistmann, D. Grady, T. Michaels & R. H. Mitchell, "Gas Gun for Impact Studies," to be published in Review of Scientific Instruments; tentative publication date - July 1970.